From Formation to Reactivation of Inactive Lithium in Lithium Metal Anodes

Abdolkhaled Mohammadi, Pedram Ghorbanzade, Juan Miguel López del Amo, Laure Monconduit, Lorenzo Stievano

ChemElectroChem

Review
doi.org/10.1002/celc.202500242

Chemistry Europe
European Chemical Societies Publishing

www.chemelectrochem.org

From Formation to Reactivation of Inactive Lithium in Lithium Metal Anodes

Abdolkhaled Mohammadi,* Pedram Ghorbanzade, Juan Miguel López del Amo, Laure Monconduit, and Lorenzo Stievano*

Inactive lithium (Li), often referred to as dead or isolated Li, consists of electrochemically disconnected metallic Li and Li-containing compounds trapped within or beneath the solid–electrolyte interphase (SEI). It is widely recognized as a primary failure mode in lithium-metal batteries (LMBs), contributing to performance degradation, safety concerns, and limited scalability. This review outlines the sequential processes of Li nucleation, growth of high-surface-area Li, and the formation of inactive Li, while identifying the key physicochemical factors influencing each stage. Li nucleation is governed by current density, temperature, electrolyte formulation, and interfacial properties, which collectively dictate the uniformity of Li plating. High-surface-area Li growth introduces mechanical and chemical instabilities, fractures and uneven stripping of these filamentous structures lead to Li isolation and inactive Li accumulation. To address these challenges, advanced characterization techniques, including solid-state nuclear magnetic resonance spectroscopy, titration gas chromatography, inductively coupled plasma optical emission spectroscopy, and operando synchrotron X-ray diffraction, offer critical insights into the formation and progression of inactive Li. Emerging reactivation strategies, such as redox mediators and tailored cycling protocols, show promise in recovering lost capacity. This review presents key mechanistic factors, advanced diagnostic tools, and emerging reactivation strategies to support a deeper understanding and control of failure mechanisms in LMBs systems.

1. Introduction

Lithium-metal batteries (LMBs) are considered one of the most promising candidates for next-generation energy storage systems due to their high energy density and capacity. With a theoretical specific capacity of 3860 mAh g^{-1} and an ultra-low reduction potential, lithium metal anodes offer significant advantages over conventional graphite-based anodes. These properties make LMBs a desirable choice for applications ranging from electric vehicles to portable electronics. However, despite their promise, the commercialization of LMBs faces critical challenges, particularly those associated with lithium metal's unique electrochemical behavior.

A major obstacle in LMB development is the formation and evolution of inactive lithium (Li), a phenomenon that significantly impairs battery performance and safety. Inactive Li encompasses both electrically isolated metallic lithium and lithium compounds encapsulated within the solid electrolyte interphase (SEI). The formation of inactive Li is closely tied to the processes of lithium nucleation and growth. During cycling, uneven Li deposition and stripping, SEI degradation, and high-surface-area Li fracture contribute to the accumulation of inactive Li, leading to reduced Coulombic efficiency (CE) and capacity loss over time.

Lithium nucleation and growth are influenced by several factors, including current density, temperature, electrolyte composition, and SEI properties. High current densities and temperature variations exacerbate uneven Li deposition, while electrolyte instability and poorly formed SEI layers promote parasitic reactions. As lithium grows into high-surface-area structures, the risk of short circuits and thermal runaway increases, posing significant safety concerns. Moreover, high-surface-area fracture and mechanical instability result in the isolation of metallic Li, which subsequently becomes inactive and trapped beneath the SEI layer.

Quantifying and understanding the formation of inactive Li are essential for addressing these challenges. Advanced characterization

A. Mohammadi, L. Monconduit, L. Stievano
ICGM
CNRS
ENSCM
Univ. Montpellier
34090 Montpellier, France
E-mail: kmohammadi@basquevolt.com
lorenzo.stievano@umontpellier.fr

A. Mohammadi, L. Monconduit, L. Stievano
RS2E
CNRS
80000 Amiens, France

A. Mohammadi, P. Ghorbanzade, L. Monconduit, L. Stievano
Alistore-European Research Institute
CNRS
80039 Amiens, France

P. Ghorbanzade, J. M. López del Amo
Centre for Cooperative Research on Alternative Energies (CIC energiGUNE)
Basque Research and Technology Alliance (BRTA)
01510 Vitoria-Gasteiz, Spain

P. Ghorbanzade
Department of Organic and Inorganic Chemistry, Faculty of Science and Technology
University of Basque Country (UPV/EHU)
48940 Leioa, Spain

techniques, such as solid-state nuclear magnetic resonance (NMR) spectroscopy, titration gas chromatography (TGC), inductively coupled plasma optical emission spectroscopy (ICP-OES), and *operando* synchrotron X-ray diffraction (XRD), have provided valuable insights into the mechanisms and dynamics of inactive Li formation. These methods allow for precise monitoring of inactive Li evolution, particularly in practical cell configurations such as pouch cells, bridging the gap between laboratory research and commercial applications.

Emerging strategies aimed at mitigating and reactivating inactive Li include the use of redox mediators and tailored electrochemical cycling protocols. These approaches not only enhance Coulombic efficiency but also extend the cycle life of LMBs, moving the technology closer to practical implementation. Furthermore, advances in surface and interface engineering, along with electrolyte optimization, have shown promise in controlling Li deposition and suppressing high-surface-area Li growth.

This review focuses on the interconnected processes of Li nucleation, deposition, and inactive Li formation, emphasizing the underlying mechanisms and the role of critical parameters. Additionally, it highlights state-of-the-art quantification techniques and innovative reactivation strategies, offering a comprehensive perspective on overcoming the challenges associated with inactive Li. By addressing these key issues, this work aims to provide a roadmap for advancing LMB technologies, paving the way for safer, more efficient and commercially viable energy storage systems.

2. High-Surface-Area Lithium Growth

The formation of high-surface-area Li is the most critical obstacle in developing safe rechargeable LMBs. Many studies collectively refer to all forms of high-surface Li deposits as "Li dendrites," given their detrimental impact on safety and capacity retention

Abdolkhaled Mohammadi is an Anode R&D Engineer at Basquevolt. He received his Ph.D. in Chemistry and Physico-Chemistry of Materials in 2023 as a joint student at Université de Montpellier, Institut Charles Gerhardt Montpellier (ICGM) and Uppsala University within the European ALISTORE-ERI network, under the supervision of Dr. L. Monconduit, Prof. L. Stievano, and Prof. R. Younesi. His research focuses on lithium metal and anode-free batteries, with emphasis on lithium surface modification, electrolyte engineering, and the influence of key parameters on cell performance, including pressure, formation protocols, and post-mortem analysis.

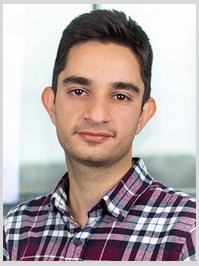

Pedram Ghorbanzade is a researcher in the NMR group at CIC energiGUNE (Vitoria-Gasteiz, Spain). He obtained a B.Sc. in Polymer Engineering from the University of Tehran (2018) and an Erasmus Mundus Master's degree (2021) in Materials for Energy Storage and Conversion (MESC+). In March 2025, he defended his Ph.D., carried out within the European DESTINY program under the supervision of Dr. Juan Miguel López del Amo. His research focuses on composite solid electrolytes, with emphasis on interfacial ion transport and characterization using solid-state NMR and electrochemical techniques.

Juan Miguel López del Amo obtained his Chemistry degree in 2000 (University of Seville) and a Ph.D. in 2006 (Free University of Berlin) under Prof. H.H. Limbach and Prof. G. Buntkowsky, focusing on solid-state NMR studies of hydrogen transfer and isotope effects. He then pursued postdoctoral research at FMP-Berlin and the Helmholtz Centre Munich with Prof. B. Reif, applying solid-state NMR to protein structure and pharmacology-related amyloid studies. Since 2012, he has led the solid-state NMR platform at CIC energiGUNE, where he investigates electrodes and electrolytes for batteries and supercapacitors using advanced and operando solid-state NMR techniques.

Laure Monconduit is Research Director at CNRS, working at the ICGM, Université de Montpellier. She received her Ph.D. in Chemistry from the University of Nantes in 1995 and completed postdoctoral research at the Max Planck Institute in Stuttgart in 1996. She became CNRS Research Director in 2011 and has since led the "Batteries" research group. Her research explores Li-ion and post-lithium (Na, K, Mg, Ca) batteries, electrode/electrolyte interfacial processes, solid-state batteries, and recycling strategies, with emphasis on operando techniques. She is active in RS2E and ALISTORE-ERI, has authored over 200 publications, 13 patents, and 8 book chapters.

Lorenzo Stievano is Distinguished Professor of Chemistry at Université de Montpellier and conducts research at ICGM. After earning his Ph.D. in Chemical Sciences from the University of Ferrara in 1999 and postdoctoral work in France, he became Associate Professor at Sorbonne Université before joining Montpellier in 2009. His research focuses on electrochemical energy storage systems, from Li-ion to post-lithium batteries, studied by in situ and operando spectroscopy, as well as innovative recycling strategies. He co-directs the European network Alistore-ERI, coordinates RS2E characterization platforms, and is Fellow of the Royal Society of Chemistry.

in LMBs.[1–5] The substantial surface area of these plated Li structures accelerates parasitic reactions with the electrolyte, resulting in the irreversible consumption of Li metal and electrolyte. Consequently, the electrolyte may be fully depleted, and CE will decline sharply. Furthermore, these microstructural Li deposits can easily lose electrical contact with the bulk Li or the current collector during stripping, becoming inactive Li and causing severe capacity loss. Hence, preventing high-surface-area Li growth is pivotal for developing the next generation of high-energy-density and safe LMBs.

Since the 1960s, researchers have recognized the formation of high-surface-area Li, but the underlying growth mechanisms are still not fully understood.[1,6] Although theoretical models can describe how high-surface-area Li initiates and evolves, their accuracy often suffers from oversimplified assumptions. For example, most models overlook the influence of the SEI during Li plating. Recent scientific findings indicate that suppressing high-surface-area Li requires understanding the morphology of Li deposits at each growth stage.[7] Indeed, Li deposits can exhibit diverse forms, from needle- or whisker-like dendrites to mossy structures,[2] and their specific shape directly affects the cycling performance. While parameters such as temperature, pressure, and current density play a role in determining Li morphology, the electrolyte system is arguably the most critical factor in forming a stable and uniform SEI. This SEI serves as a protective barrier that improves cycling efficiency.

Over the years, several theoretical models have been proposed to better understand the formation and growth of high-surface-area Li. The Monroe and Newman model focuses on the role of chemical potential differences caused by surface curvature during lithium deposition on polymer electrolytes.[8] According to their theory, protrusions with higher curvature experience preferential growth due to local increases in deposition kinetics, which was later confirmed experimentally. Meanwhile, the Chazalviel model emphasizes ion transport limitations,[9] predicting that when the current density exceeds a critical threshold, ion depletion near the electrode leads to the formation of space charge regions, initiating dendrite growth. This model successfully explains the relationship between current density, electrolyte properties, and the onset of dendritic structures. Alternatively, Yamaki et al. propose a distinct mechanism involving lithium extrusion through defects in the SEI under internal pressure, resulting in whisker-like morphologies growing from the base rather than the tip.[10] Together, these models demonstrate that dendrite growth is governed by a complex interplay of electrochemical kinetics, ion transport, mechanical stresses, and interfacial stability.

In the following sections, these observed morphologies are discussed in greater detail, highlighting the fundamental processes that govern their development with the support of advanced characterization techniques.

2.1. Initial Nucleation

A clear understanding of the initial nucleation process of high-surface-area Li is pivotal for preventing the formation of inhomogeneous surface structures during Li plating.[1] In LMBs, Li repeatedly plates and strips, and nucleation can occur under diverse conditions during each cycle. Recent studies highlight how factors such as current density, temperature, electrode substrate, and the nature of the SEI collectively influence nucleation behavior.[11] **Figure 1** illustrates that Li atoms migrate from the electrolyte and cluster on the metal surface, forming embryonic

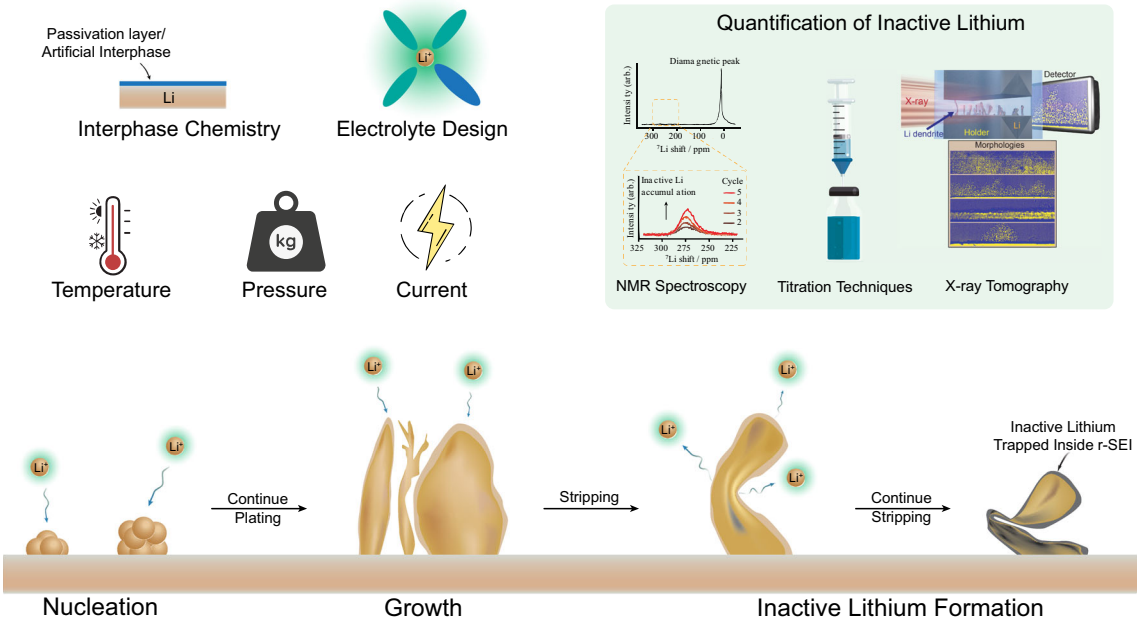

Figure 1. Overview of lithium growth and inactive Li formation in LMBs. Factors like current, pressure, temperature, and interphase chemistry influence morphology. Quantification methods (e.g., NMR, titration, XCT) assess inactive lithium.

nuclei that eventually evolve into high-surface-area deposits. By pinpointing the role of these parameters and visualizing the early stages of Li nucleation, it is possible to better engineer conditions that promote uniform Li deposition, thereby enhancing battery performance and safety.

2.1.1. Influence of Current Density

Current density is a critical parameter influencing the nucleation behavior and growth morphology of high-surface-area Li, as it dictates the rate of Li^+ transport and deposition kinetics at the electrode surface.[12] For example, Pei et al.[13] investigated the size, shape, and areal density of Li nuclei formed on planar Cu electrodes and how these attributes vary with current density. Using in situ SEM during the plating process (up to 0.1 mAh cm^{-2}) at different current densities, they observed that higher current densities lead to smaller, more densely packed Li nuclei across the electrode surface (**Figure 2**a). In contrast, fewer but larger Li deposits form at lower current densities, spaced out over the surface. These findings underscore the importance of controlling current density to manage the nucleation behavior and morphological evolution of Li, ultimately guiding strategies for enhancing cycling stability in LMBs.

At a fixed temperature, raising the applied current density J alters lithium nucleation through three mutually reinforcing mechanisms: I) larger kinetic overpotential, II) faster Li^+ depletion that triggers the Sand-time instability, and III) interfacial energy focusing that amplifies growth at protruding tips.

Electrochemical overpotential and critical nucleus size: During galvanostatic operation, the overpotential η is related to the current density via the Tafel expression:

$$\eta = \frac{RT}{\alpha F}\ln\left(\frac{J}{i_0}\right) \quad (1)$$

Here, α the charge-transfer coefficient ($\alpha \approx 0.5 - 1$ for Li| electrolyte interfaces), R is the universal gas constant, T is temperature, F is Faraday's constant, and i_0 is the exchange current density. As J increases, so does the magnitude of the overpotential $|\eta|$, which has a direct impact on the energetics of nucleation.

Classical nucleation theory describes the size of the critical nucleus r_c as:

$$r_c = \frac{2\gamma V_m}{nF|\eta|} \quad (2)$$

and the corresponding nucleation barrier energy ΔG_c scales as:

$$\Delta G_c \propto |\eta|^{-2} \quad (3)$$

where γ is the surface energy, $n = 1$ for $Li^+ + e^- \rightarrow Li$, and V_m is the molar volume of Li. These expressions indicate that a higher overpotential reduces both the critical nucleus size and the energy barrier, facilitating the formation of numerous smaller nuclei. This theoretical prediction aligns well with operando imaging observations showing a shift from isolated islands to dense nuclei as J increases.[8,9,13,14]

Local Li^+ concentration depletion and Sand's time: At high J, ion transport becomes a limiting factor. The maximum sustainable current density before diffusion limitations dominate is given by:

$$J^* = \frac{2eC_0D}{(1-t^+)L} \quad (4)$$

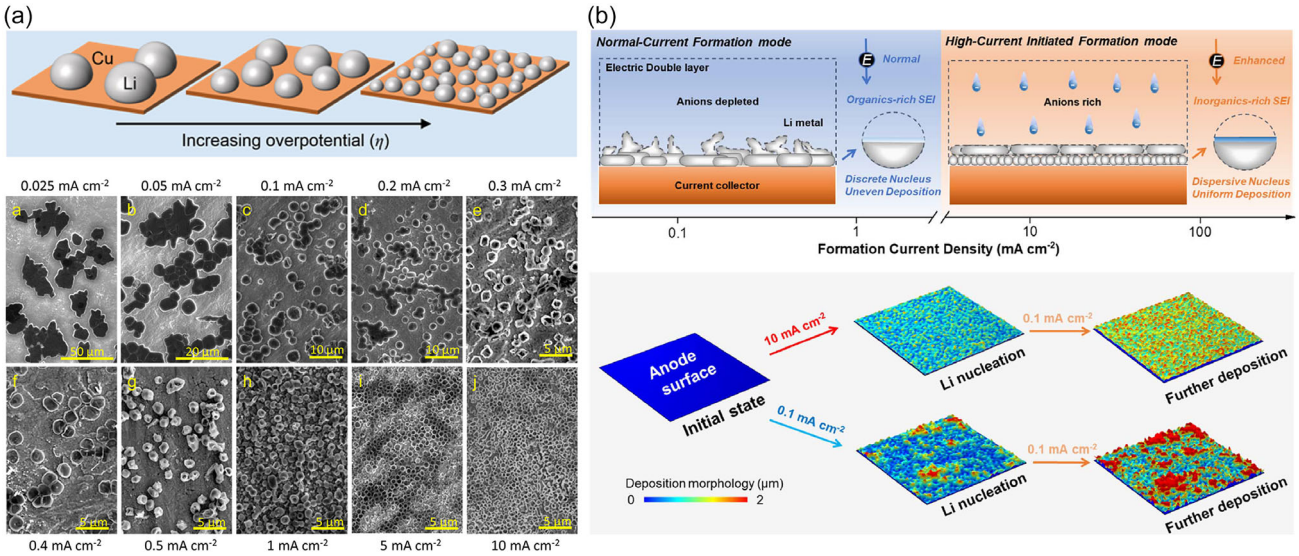

Figure 2. Impact of current density on lithium nucleation: a) schematic and ex situ SEM images showing the density and size of Li nuclei plated on copper foil at varying current densities (total areal capacity: 0.1 mA cm^{-2}). At lower current densities, the copper substrate is visible beneath sparsely distributed Li nuclei.[13] b) Schematic illustration of the morphological evolution in the first Li deposition process under a normal 0.1C formation strategy and a high-current initiated formation strategy in AFLMBs and FEM simulation results showing the Li nucleation morphology at applied current densities of 10 and 0.1 mA cm^{-2} with a deposition capacity of 0.5 mAh cm^{-2}, as well as the subsequent deposition morphology during further plating under 0.1 mA cm^{-2}.[20] Reproduced with permission.[13] Copyright 2017, American Chemical Society, and reproduced with permission.[20] Copyright 2024, Royal Society of Chemistry.

where e is the elementary charge, C_0 is the bulk Li^+ concentration, D is the diffusion coefficient, t^+ is the cation transference number, and L is the electrolyte thickness. When J approaches J^*, Li^+ ions are depleted near the interface after a finite time known as Sand's time:

$$\tau = \pi D\left(\frac{eC_0}{2J(1-t^+)}\right)^2 \quad (5)$$

Beyond this point, interfacial ion depletion leads to the formation of a space-charge layer with a strong electric field that drives ions preferentially toward protruding tips, creating a positive feedback loop for dendrite growth.[2,15–17]

Interfacial energy feedback and tip effects: During growth, the local overpotential naturally decreases as Li accumulates, promoting growth along lower-energy pathways. This causes larger or better-aligned nuclei to grow faster, a tip amplification effect. Such behavior has been reproduced in phase-field simulations that model the evolution of isolated metallic Li domains.[18,19]

Collectively, Equation (1)–(5) describe how nucleation transitions from low-density, large nuclei at moderate J to high-density, small nuclei under high J, driven by both a reduced nucleation barrier and enhanced ion gradients. If unchecked, these conditions can also promote dendritic growth. Importantly, these electrochemical and transport-driven effects operate independently of the substrate properties, complementing the substrate-specific mechanisms discussed in influence of electrode substrate section.

Although smaller Li nuclei are often associated with higher nucleation densities and a greater risk of high-surface-area Li growth, Cai et al.[20] recently demonstrated that applying very high current densities during the initial Li deposition stage can yield uniformly distributed, ultra-fine Li nanospheres, a configuration that enhances cycling stability in anode-free lithium-metal batteries (AFLMBs), often called anodeless or zero-excess LMBs. By charging the cell at current densities exceeding 10 mA cm^{-2}, an abundance of ultrafine Li nanospheres is deposited on the anode current collector, creating numerous electrochemically active sites that guide homogeneous Li nucleation and accommodate high Li stripping/plating kinetics (Figure 2b). Simultaneously, the elevated current density induces the preferential decomposition of anions, resulting in a robust, inorganic-rich SEI. Together, these effects promote two-dimensional Li growth and suppress the formation of hazardous high-surface-area Li. The use of high-current deposition enhances cycling stability in pouch cells, highlighting the practical viability of this approach.

A similar phenomenon arises under conditions of higher pit densities, which likewise fosters more uniform Li nucleation and reduces the chance of uneven growth. As it will be detailed in the following section, these pits serve as preferential sites for Li deposition, and their controlled formation can further enhance the uniformity of Li coverage. Overall, these observations indicate that smaller nucleation sizes and higher pit densities do not inherently degrade performance, but rather help to achieve uniform, dense Li deposits across the electrode surface.

According to classical nucleation theory, the formation of a solid Li phase requires overcoming a nucleation energy barrier, which is electrochemically demonstrated as the nucleation overpotential, the initial voltage dip observed at the onset of plating.[13,21,22] As illustrated in **Figure 3**a (Stage III), Li metal deposition initially undergoes a sharp voltage drop, followed by a stable voltage plateau. The nucleation overpotential can be identified as the voltage difference between this lowest point and the subsequent flat portion of the curve. This overpotential arises from contributions throughout the cell, including the counter electrode, electrolyte, and working electrode. Although many Li metal plating studies rely on a two-electrode setup that assumes negligible impact from the Li foil counter electrode, such an assumption often leads to inaccurate conclusions since the counter electrode does, in fact, contribute to the total overpotential. A three-electrode setup provides a clearer view of each electrode's role (Figure 3b). In our work,[21] the different sources of polarization during Li electrodeposition were examined and dissociated, showing that the initial nucleation overpotential primarily originates from Li stripping at the counter electrode rather than nucleation on the working electrode. These findings, which align with other recent reports,[23–25] emphasize the need to revisit conclusions drawn from two-electrode configurations and highlight the advantages of a three-electrode approach for more accurate analyses.

Sanchez et al.[26] investigated the behavior of Li electrodes under varying current densities in a symmetric Li||Li cell using operando optical microscopy. As shown in Figure 3c,i–vi, they investigated the electrode behavior under various current densities in a symmetric Li||Li cell. Their results revealed a positive correlation between current density and the nucleation density of both high-surface-area Li (i.e., dendrites) and pits. Interestingly, they found that the nucleation density for pits consistently exceeded that of high surface area Li at all current densities (Figure 3c,vii). Notably, pits form during Li stripping from the bulk Li surface. Drawing on these observations, Sanchez et al. concluded that dense Li growth, typically more demanding, could be mitigated by reducing the current density. Furthermore, they determined that Li nucleation is closely tied to defect sites, such as grain boundaries, which act as preferential nucleation spots. Additionally, they suggested that local variations in the SEI, influenced by grain boundaries and other defect sites, may cause these preferential nucleation behaviors.

2.1.2. Influence of SEI

Beyond current density, the composition of the SEI forming upon contact with the electrolyte also plays a significant role in governing initial Li nucleation. According to Biswal et al.,[17] both bulk ion diffusion and the transport properties of SEI are crucial in governing Li nucleation and growth. In their study, Li was plated at various current densities in carbonate-based electrolytes, both with and without fluoroethylene carbonate (FEC) additives. The inclusion of FEC altered the SEI, increasing its fluorine content and enhancing its surface properties, such as interfacial energy and

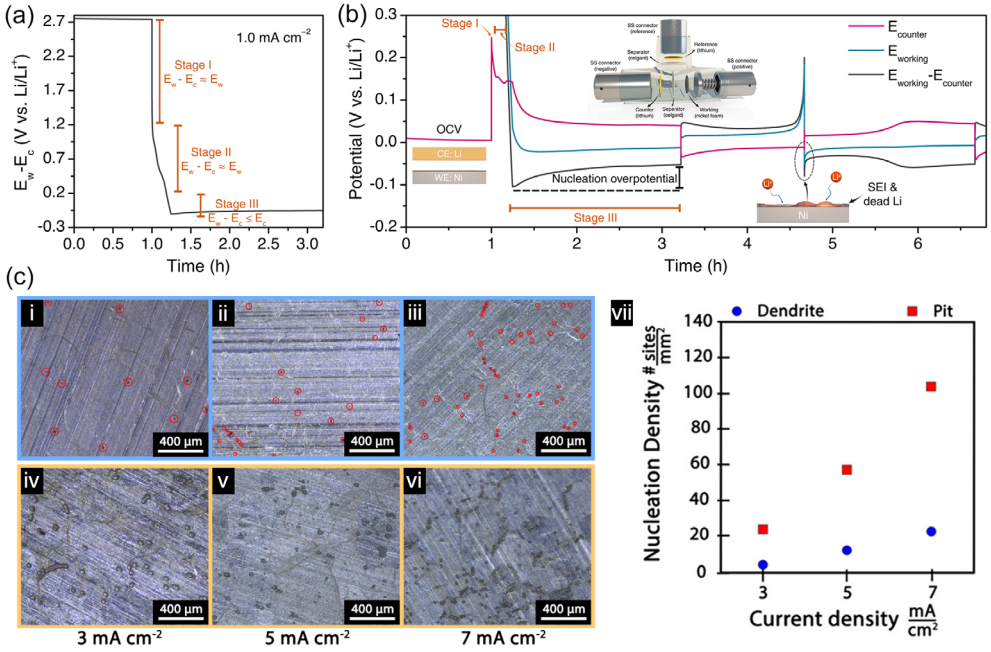

Figure 3. Origin of nucleation overpotential: a) electrochemical potential curve for half-cycle Li electrodeposition, divided into three stages: Stage I, potential changes dominated by working electrode; Stage II, SEI formation; and Stage III, nucleation overpotential dominated by the counter electrode. b) Deconvoluted potential profiles of the working and counter electrodes during plating and stripping at 1.0 mA cm^{-2}, highlighting the dominance of the counter electrode in nucleation overpotential inset is schematic of the Swagelok three-electrode cell.[21] c) Optical images of the working electrode surface after Li deposition (i–iii) and subsequent stripping (iv–vi) at different current densities, deposition corresponds to 0.0025 mAh cm^{-2}, while stripping corresponds to 0.2 mAh cm^{-2}. Red circles in (i–iii) highlight Li nucleation sites, Graph (vii) shows the nucleation density of both pits and high-surface-area Li as a function of current density.[26] Reproduced with permission.[21] Copyright 2022, Electrochemical Society, and reproduced with permission.[26] Copyright 2020, American Chemical Society.

ion diffusivity. This modification resulted in smoother and more uniform Li deposition. Higher FEC concentrations led to the formation of flatter and slightly larger Li nuclei on stainless steel substrates, as observed in **Figure 4**a via SEM. This suggests that FEC facilitates a LiF-rich SEI, which lowers surface ion diffusion barriers and promotes uniform nucleation.

Gu et al.[27] show how the intrinsic properties of the SEI, particularly its ionic conductivity and Li^+ transference number, dictate the Li^+ transport mechanism during deposition. They demonstrate that the SEI's ionic conductivity and Li^+ transference number are particularly critical in the early stages of Li nucleation and growth. SEIs with lower ionic conductivity and transference numbers induce a shift in the Li-ion transport mechanism. As illustrated in Figure 4b, the Li^+ transport mechanism transitions between two regimes: a SEI-controlled regime at the early stages and an electrolyte-controlled regime as deposition progresses.

In the initial SEI-controlled regime (Stage I), Li^+ transport is dominated by electromigration through the SEI. The limited ionic conductivity and low Li^+ transference number within the SEI result in a buildup of ions at the electrode/SEI interface. This leads to the formation of a space-charge layer (SCL), as depicted in the schematic, where ion accumulation occurs near the interface due to the limited ability of the SEI to facilitate efficient ion movement. This accumulation promotes the growth of high-surface-area Li structures, such as dendrite embryos, that eventually compromise the SEI's structural integrity. Once the SEI breaks (Stage II), Li^+ transport shifts to the electrolyte-controlled regime, where diffusion becomes the primary transport mechanism. This transition is marked by significant morphological changes, as shown by SEM (Figure 4b,i–iii). Initially, uniform spherical deposits dominate the SEI-controlled regime. However, as SCL develops and SEI integrity degrades, irregular Li morphologies emerge. SEM images highlight how these transitions are associated with a decrease in deposition uniformity and the initiation of dendritic growth.

Together, these findings highlight the importance of tailoring SEI properties to facilitate uniform Li nucleation and suppress the formation of high-surface-area Li that undermines cycling stability in LMBs.

2.1.3. Influence of Temperature

Temperature profoundly affects Li nucleation and SEI by altering Li^+ diffusion and surface reaction kinetics. This change is primarily due to enhanced lithiophilicity and increased Li^+ diffusion coefficients at higher temperatures. Yan et al.[28] demonstrated that at 60 °C, Li deposition occurs as sparse, large nuclei, yielding a compact, dendrite-free morphology. In contrast, at lower temperatures, around 20 °C or below, the number of nuclei rises sharply, producing smaller, more crowded deposits that elevate the likelihood of dendrite growth. SEM images in **Figure 5**a vividly illustrate this progressive shift, showing how small, densely packed nuclei at 0 °C evolve into larger, sparse nuclei at 60 °C, emphasizing the critical role of temperature in deposit morphology.

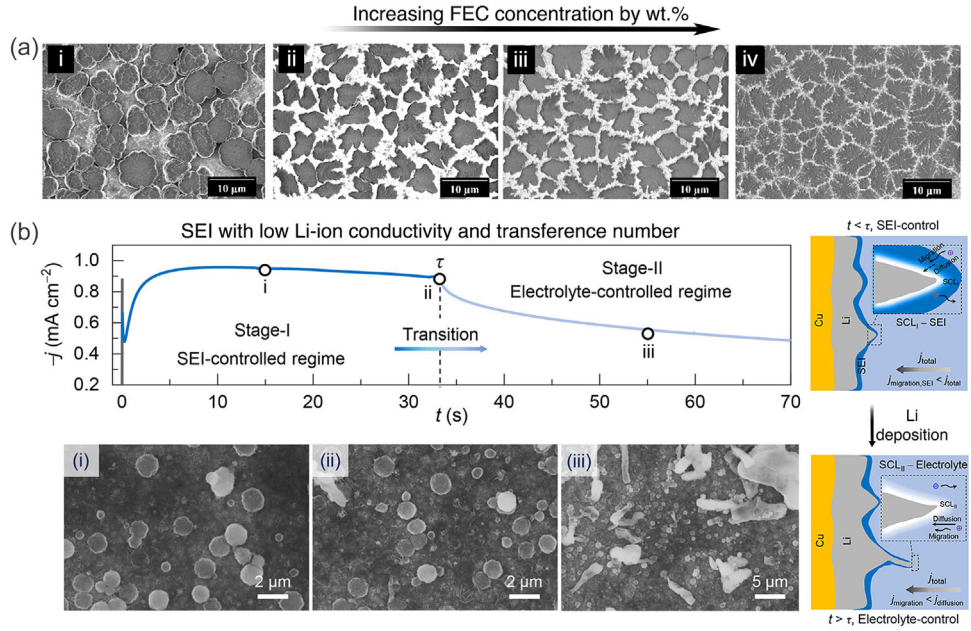

Figure 4. Impact of SEI properties on lithium nucleation: a) SEM images showing the effect of increasing FEC concentration on Li nuclei morphology and density at 0.5 mA cm^{-2} in a 1 M $LiPF_6$ EC/DMC (1:1 vol%) electrolyte: i) 0 wt%, ii) 10 wt%, iii) 30 wt%, and iv) 50 wt%, under the Li nuclei can be seen the bare bright stainless steel substrate.[17] b) Transition in Li-ion transport control during deposition on Cu substrates, with suboptimal SEI properties (low ionic conductivity and Li-ion transference number). The electrochemical curve illustrates the two stages: Stage I (SEI-controlled regime), where ion transport is dominated by the SEI, and Stage II (electrolyte-controlled regime), following SEI breakdown. SEM images depict morphological changes during the stages: i) SEI-controlled regime, ii) transition with SEI breakage, and iii) electrolyte-controlled regime. A schematic shows the formation of a SCL at the electrode/SEI interface, driving the transition in control from the SEI to the electrolyte.[27] Reproduced with permission.[17] Copyright 2019, American Chemical Society and reproduced with permission.[27] Copyright 2023, American Chemical Society.

Beyond nucleation behavior, SEI structure also evolves with temperature. Wang et al.[29] shows that at 20 °C in ether-based electrolytes, the SEI predominantly comprises an amorphous polymeric layer, which is fragile and highly soluble in the electrolyte (Figure 5b,top). This inadequate passivation triggers ongoing side reactions and non-uniform Li deposition. However, at 60 °C, the SEI transforms into a robust, multilayered film, featuring an outer Li_2O layer (Figure 5b,bottom). This enhanced structure improves mechanical integrity and effectively passivates the electrode surface, reducing parasitic reactions and enabling higher Coulombic efficiencies and improved cycling stability. Nevertheless, the temperature-dependent behavior of the SEI may vary according to the electrolyte composition. In additive-free carbonate-based electrolytes, elevated temperatures can produce thicker, more heterogeneous SEI layers, ultimately increasing impedance and degrading cycle life. By contrast, ether-based electrolytes often benefit from higher temperatures, attaining superior performance and stable SEI formation. Overall, operating temperature is pivotal for dictating Li-deposit morphology and SEI characteristics. While higher temperatures generally promote more uniform deposition and improve cycling performance, selecting the right electrolyte composition and operating conditions is crucial to fully capitalize on these thermal benefits.

2.1.4. Influence of Electrode Substrate

After the reduction process, the resulting metal atoms gather in a cluster of small nuclei that aid further deposition, accompanied by a rise in surface free energy and a reduction of the bulk free energy.[30,31] Whether the nuclei are stable or unstable depends on the net change in the total free energy. It is common for crystalline nuclei to be heterogeneously distributed, as their formation is influenced by the substrate morphology and the presence of impurities. This process is known as heterogeneous nucleation. If the shape of a given nucleus is assumed to be a spherical dome with a radius of r (**Figure 6**a), the critical free energy ΔG^*_{eq} can be derived based on the classical heterogeneous nucleation theory:[30,31]

$$\mathrm{Cos}\theta = \frac{\gamma_{SE} - \gamma_{SN}}{\gamma_{NE}} \tag{6}$$

$$\Delta G^*_{eq} = \frac{1}{3}\left(4\pi r^*_{eq}2\right)\gamma_{NE}\left(\frac{2 - 3\cos\theta + \cos^3\theta}{4}\right) \tag{7}$$

where θ is contact angle, r_{eq}^*, γ_{SE}, γ_{SN}, and γ_{NE} are critical nucleus radius, substrate–electrolyte, substrate–nucleus, and nucleus–electrolyte interfacial free energy, respectively. The required nucleation free energy is zero when $\theta = 0$, and the same as in homogeneous nucleation when $\theta = 180°$. Consequently, improving the wettability of metal nuclei on substrates can reduce θ and lower the nucleation free energy. Therefore, the properties of the substrates have a significant impact on the electroplating behavior of metals in an aqueous solution. While lowering γ via lithiophilic coatings reduces the initial nucleation barrier, the ultimate plating morphology also depends on the current-density-induced overpotential and Li^+ transport limitations described in influence of current density section.

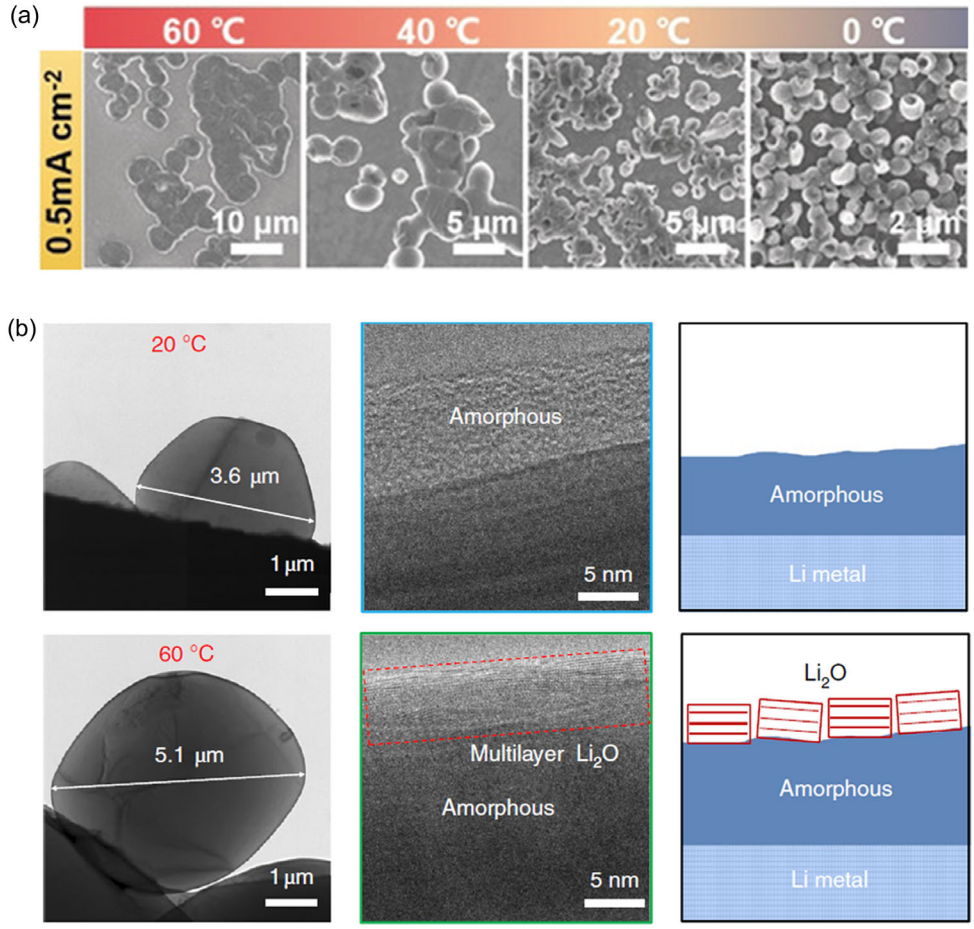

Figure 5. Impact of temperature on lithium nucleation: a) SEM images of Li nuclei layers plated at temperatures ranging from 0 to 60 °C on the surface of a copper electrode in 1.0 M LiTFSI in DOL/DME (1:1 vol.) with 1 wt% $LiNO_3$ electrolyte at a current density of 0.5 mA cm^{-2} and a capacity of 0.1 mAh cm^{-2}.[28] b) Cryo-EM images and corresponding schematics of Li deposits formed at 20 °C (top row) and 60 °C (bottom row) with a deposition capacity of 0.4 mAh cm^{-2} at a current density of 1 mA cm^{-2}. At 20 °C, an amorphous polymeric SEI layer (≈20 nm) is formed, while at 60 °C, a thicker (≈35 nm) multilayered SEI structure with an outer crystalline Li_2O layer is observed, contributing to enhanced passivation and mechanical stability.[29] Reproduced with permission.[28] Copyright 2019, John Wiley and Sons, and reproduced with permission.[29] Copyright 2019, Springer Nature.

Yan et al.[32] investigated various types of Li nucleation on different metal substrates and found that the substrate strongly dictates the resulting deposition pattern. While some metals (e.g., Pt, Al, Mg, Zn, Ag, and Au) easily alloy with Li, others (e.g., Cu, C, and Ni) do not. To illustrate the substrate effect, they compared Au and Cu as current collectors. As shown in Figure 6b, Li is more readily retained on Au, favoring a more uniform deposit. Therefore, selecting appropriate substrate materials helps ensure a desirable mode of heterogeneous nucleation and smooth electroplated Li growth.

In our previous study,[33] it was shown that lithiophilic coatings, such as zinc oxide (ZnO), significantly enhance the uniformity of Li nucleation, resulting in more consistent and homogeneous Li deposition (Figure 6c–g). SEM images of ZnO-coated nickel foam reveal that Li nucleation is evenly distributed across the entire 3D foam structure, highlighting the effectiveness of this surface modification (Figure 6d). In contrast, Li nuclei on bare nickel form unevenly, aggregating into localized clusters, as shown in Figure 6e. The improved morphology on the ZnO-coated substrate is attributed to the interaction between Li ions and the ZnO layer, which undergoes a conversion reaction to form a LiZn–Li_2O composite during the first steps of lithiation. This composite layer not only promotes smoother and more uniform nucleation but also mitigates high-surface-area Li formation (Figure 6g). These findings emphasize the critical role of surface modifications like ZnO coatings in achieving controlled Li nucleation and improving the performance and safety of LMBs.

In summary, homogeneous nucleation is critical for achieving smooth Li electrodeposition. Accordingly, particular attention should be paid to parameters such as current collector, SEI composition, applied current density, and operating temperature, all of which significantly influence the nucleation process.

2.2. Lithium Growth after Nucleation

Following the nucleation, Li growth continues and assumes various kinds of morphologies. The shape and structure of the elongated high-surface-area Li can affect cell performance and are influenced by factors such as the deposition mechanism. Although all Li growth patterns are often described under the

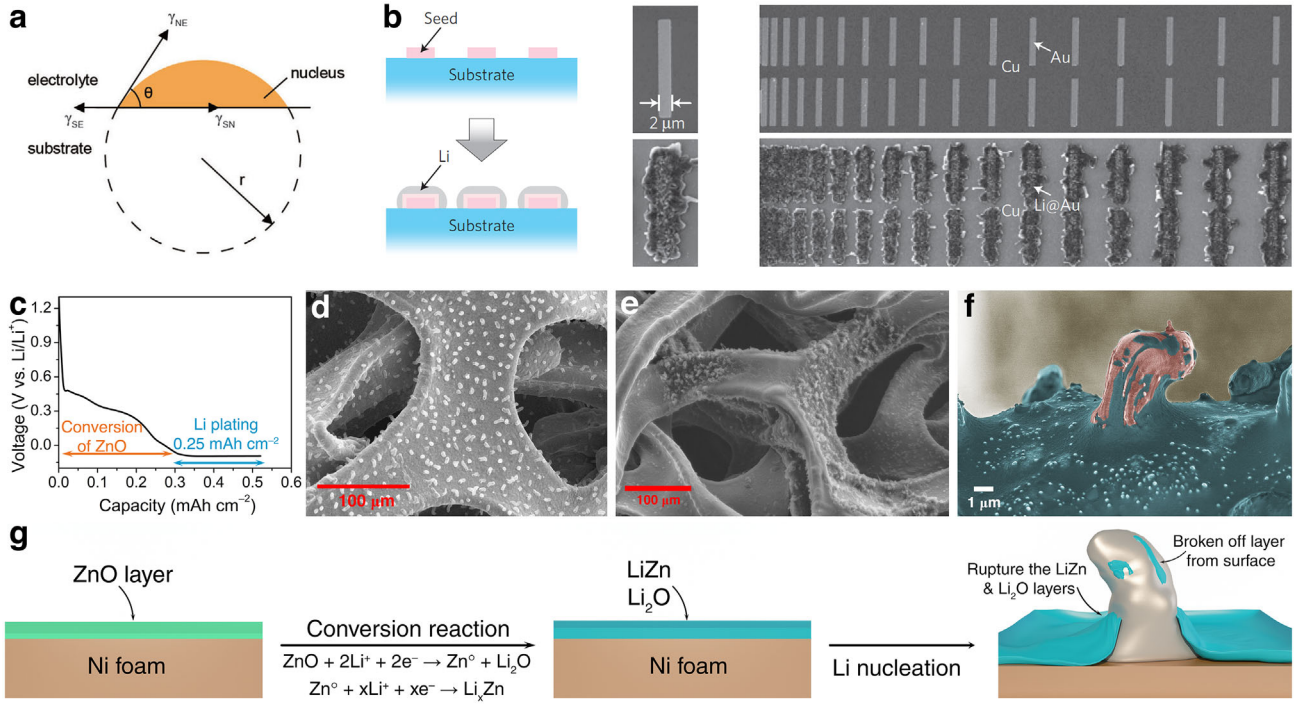

Figure 6. Impact of substrate modification on lithium nucleation: a) schematic illustrating heterogeneous nucleation with a spherical crown nucleus, highlighting interfacial energies between the nucleus, substrate, and electrolyte.[30,31] b) Schematics and SEM images showing the gold-seed-modified copper substrate before and after Li deposition. Li was observed to selectively deposit on gold strips (bottom row), illustrating substrate-dependent nucleation behavior.[32] c) Voltage profiles for the conversion of ZnO to Li_2O/LiZn followed by Li plating at a capacity of 0.25 mAh cm^{-2} and current density of 0.5 mAh cm^{-2}. d) SEM image showing uniform Li deposition on a ZnO-coated nickel foam substrate. e) SEM image of Li deposition on a pure nickel foam substrate. f) High-resolution SEM image showing ruptures in the LiZn and Li_2O layers due to Li nucleation. g) Schematic mechanism of Li deposition on a ZnO-coated nickel foam substrate, emphasizing the formation of Li_2O and LiZn layers through a conversion reaction and the subsequent Li nucleation beneath these protective layers.[33] Reproduced with permission.[31] Copyright 2020, John Wiley and Sons, and reproduced with permission.[33] Copyright 2022, Royal Society of Chemistry.

generic term "dendrite," there are, in fact, three distinct main morphologies: whiskers, mosses, and dendrites (**Figure 7**a).[34–37]

Whiskers: Also known as Li filaments or Li needles, they constitute the simplest form of Li growths, protruding from the anode in both vertical and radial directions with a few side branches.[2,37] The growth along the vertical axis is much more prominent and can reach tens of micrometers in length. This metallic Li crystal morphology is the largest of the three types of Li deposits (Figure 7a,i).

Moss: It is a wool-like mass of intertwined filaments that grow in all directions. Compared with whiskers and dendrites, moss-like Li has a larger diameter but smaller length (Figure 7a,ii).[2,34] This type of mossy growth can expand the interface area and accelerate electrolyte decomposition. Moreover, parts of the moss structure can become electrically isolated from the current collectors during dissolution. This reduction in active material is known as the accumulation of inactive Li (often called "dead/isolated Li" in the literature).[1,38]

Dendrites: Dendrites are thin branches that grow in a fractal pattern above the critical current density.[36] Bai et al.[35] took in situ images of Li plating in a Li||Li symmetric cell in a glass capillary with conventional electrolytes at different current densities. At a high current density, they observed a distinct transition from an earlier mossy-like deposit to a more rapid fractal-like growth that is classified as dendrite growth (Figure 7a,iii).

In addition, Frenck et al.[36] elucidated how the shear modulus of the electrolyte and the normalized current density define a morphology map for Li protrusions, classifying growth into whiskers, moss, dendrites, globules, and cracks (Figure 7b). This map underscores the influence of both mechanical properties and electrochemical operating conditions on Li growth. For instance, whiskers and mossy structures typically occur under lower shear modulus and moderate current densities, while dendritic growth becomes more prominent at higher normalized current densities. By highlighting these distinct regions, the authors emphasize the importance of tuning electrolyte properties and operating parameters to suppress dendritic growth and mitigate associated risks, such as internal short circuits and capacity loss, ultimately improving the safety and longevity of LMBs.

2.2.1. Influence of Current Density

Similar to Li nucleation, the Li growth morphology can also be significantly affected by the current density since it can change the Li^+ mass transfer rate associated with the electrodeposition, Li^+ bulk concentration, and the state of the SEI layer, depending on the Li salt.[1] In a recent study, Liu et al.[39] examined the relationship between exchange-current density and high-surface-area Li growth. Exchange-current density represents the magnitude of

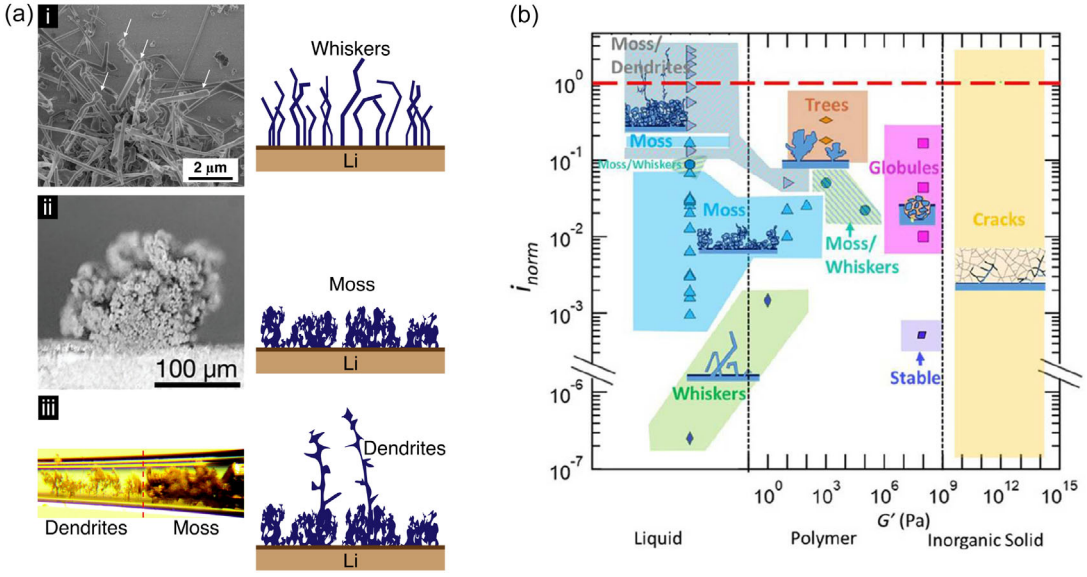

Figure 7. High-surface-area lithium deposition morphology: a) SEM images and schematic representation showing the main typical morphologies of electrodeposited Li: i) whiskers,[37] ii) moss,[34] and iii) dendrites.[35] b) morphological classification of Li deposits as a function of the current density normalized by the limiting current density, i_{norm}, versus the electrolyte type and storage shear modulus, G′, illustrating transitions between stable, whisker, moss, dendrite, and other type of Li deposition.[36] Reproduced with permission.[35] Copyright 2016, John Wiley and Sons, and reproduced with permission.[36] Copyright 2019, Frontiers Media SA.

both anodic and cathodic reaction rates under equilibrium conditions. The study demonstrates that the electrodeposition behavior of Li is highly dependent on the exchange current density at the surface of the electrode, as shown in **Figure 8**a. Low exchange current density leads to dense Li electrodeposition with a low aspect ratio and fewer columnar structures, whereas high exchange current density promotes dense needle-like growth of high-surface-area Li.

In a separate study, Boyle et al.[40] examined the impact of current density on Li deposition and identified three distinct regimes (Figure 8b): 1) At low current densities (below ≈1 mA cm^{-2}), Li tends to plate at buried Li||SEI interfaces, leading to more uniform, compact deposits with minimal high-surface-area Li formation; 2) at moderate current densities (around 1–4 mA cm^{-2}), SEI breakdown occurs, exposing fresh Li||electrolyte interfaces, resulting in nonuniform growth and the onset of high-surface-area Li formation; and 3) at high current densities (greater than ≈100 mA cm^{-2}), rapid SEI breakdown leads to the formation of faceted Li structures, such as rhombic dodecahedra, as Li plates

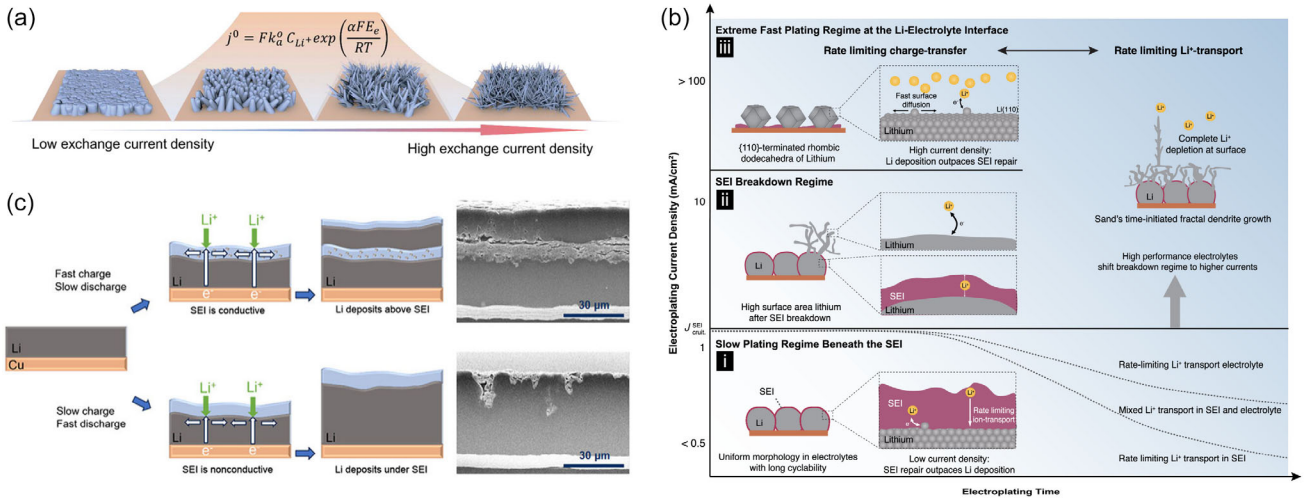

Figure 8. Impact of current density on lithium growth: a) illustration of Li electrodeposition at varying exchange current densities.[39] b) Mechanistic insight into the current-dependent regimes of Li electroplating: the slow plating regime dominated by ion transport in the SEI, the SEI breakdown regime, and the extremely fast plating regime where charge transfer at the li-electrolyte interface becomes rate-limiting.[40] c) Schematic and cryo-SEM images showing lithium deposition under asymmetric cycling; fast charge + slow discharge results in Li plating above a conductive SEI, forming a porous layer and slow charge + fast discharge promotes sub-SEI plating beneath an intact SEI, yielding denser, more stable deposits.[41] Reproduced with permission.[39] Copyright 2021, John Wiley and Sons, and reproduced with permission.[40] Copyright 2019, and reproduced with permission.[41] Copyright 2025, American Chemical Society.

predominantly at fresh Li||electrolyte interfaces. This study emphasizes that the formation of faceted rhombic dodecahedra at such extremely high current densities (e.g., 1000 mA cm^{-2}) indicates a significant shift in the electroplating mechanism. These faceted Li structures, typical of body-centered cubic growth, represent a shift in the electroplating mechanism from filamentary to a more defined, crystalline growth. However, despite reducing the typical filamentary morphology associated with high-surface-area Li, this faceted growth can still destabilize the surface and degrade battery performance under fast charging conditions.

Bai et al.[35] further illustrated the current-dependent transition from mossy to dendritic Li growth. At higher current densities, the system surpasses Sand's capacity, the point at which the Li^+ concentration at the electrode–electrolyte interface drops to zero due to diffusion limitations. This depletion leads to a sharp increase in overpotential promoting rapid, tip-driven dendritic growth. Visually, this transition is marked by the replacement of mossy lithium deposits with sharp, needle-like structures. While the influence of charging rates on the decomposition of the SEI as well as on the Li structure/morphology remains unclear due to other factors such as electrolyte composition and anode type, it is evident that as current increases, Li^+ transport within the electrolyte becomes the critical factor. When the current exceeds the diffusion limit for Li^+ transport through SEI, significant overpotential can lead to SEI breakdown, triggering the growth of high-surface-area Li at the rupture site.

Complementary insights are provided by Zhang et al.[41] who systematically decoupled the charge- and discharge-current densities in Li||NMC full cells and uncovered two dominant plating scenarios (Figure 8c): 1) Slow charge ($\leq$0.2C) + fast discharge ($\geq$1C) $\rightarrow$ sub-SEI plating. Li^+ migrates through an intact, ion-conducting SEI and nucleates directly on the metal surface, so the interphase is reused rather than rebuilt. Cryo-SEM cross-sections reveal a continuous SEI covering a dense Li layer at both 100% and 0% state of charge, delivering a high CE ($\approx$99.7%) and >700 stable cycles. 2) Fast charge ($\geq$1C) + slow discharge ($\leq$0.33C) $\rightarrow$ top-SEI plating. The SEI becomes electronically percolating; electrons reach the electrolyte side, so Li nucleates on top of the SEI, forming a thick, porous multilayer film that grows each cycle. The resulting CE falls to $\approx$98%, and cycle life shortens to $\approx$160 cycles.

They attribute this switch to the evolving SEI's ionic-to-electronic conductivity ratio (σ_i/σ_e): slow-charge/fast-discharge keeps σ_i/σ_e high, forcing ion-transport-limited nucleation beneath the film, whereas the opposite protocol lowers σ_i/σ_e by accumulating inactive Li, enabling electronic percolation and top-SEI nucleation.

Taken together, these studies show that both the absolute current density and the asymmetry between plating and stripping currents dictate whether the SEI is preserved or rebuilt. Exploiting slow-charge/fast-discharge protocols to promote Li plating beneath a reusable SEI offers a practical route to extend LMBs life without altering materials, further underscoring current density as a powerful handle for interphase and morphology engineering.

2.2.2. Stress-Driven Li Growth

Besides ionic concentration and electric field, the stress field around the metal anodes can also greatly affect Li metal deposition morphology.[1,2] Since Li metal is soft and mechanically fragile, it is sensitive to mechanical stress. There are two types of stress affecting the morphology of deposited Li: internal and external. The source of internal stress in a cell can be the considerable volume change during the plating process and the inhomogeneous deposition rate, which stresses the plated Li metal. External stress is caused by the surrounding solid interfaces, such as SEI and the separator. Recently, Kushima et al.[42] proposed a model to show the effect of the SEI layer and internal stress on the Li deposition behavior, as illustrated in **Figure 9**a. At first, the surface is covered with spherical Li nuclei, which are highly reactive and, therefore promptly covered with the SEI layer (stage 1). In the second stage, the initial deposition is pushed aside by Li whiskers sprouting from the root. This is due to the SEI layer being thinner around the root, allowing Li-ion to deposit at a higher diffusion rate at the root (stage 2). Later, the growth rate slows down since the SEI layer begins to thicken on the new Li deposition layer (stage 3). Finally (stage 4), a kink emerges on the whisker. The mounting stress caused by the SEI layer divides the whisker into two segments. The newly formed segment continues to grow from the root, pushing out the pre-existing portion of the whisker, which remains at the same diameter.

Li plating and Li stripping processes are specifically susceptible to external stress as well.[43,44] During the Li plating process, the tip/front of the Li protrusions is directly in contact with the external pressure; therefore, deposited Li is physically suppressed due to the stress force. The dynamic behavior of lithium whiskers under external stress was captured using an atomic force microscope integrated with an environmental transmission electron microscope setup.[45] This study, as illustrated in Figure 9b, demonstrates three distinct scenarios induced by external pressure. (i–iii) Buckling: the whisker bends due to compressive stress, which affects its vertical growth trajectory and structural integrity. (iv–vi) Cessation of axial growth and lateral expansion: under sustained pressure, axial growth halts, and the whisker starts to expand laterally, forming a broader Li particle. This phenomenon occurs due to the redistribution of lithium deposition from the whisker tip to its sides, driven by the increased force at the interface. (vii–ix) Kinking: the stress at the whisker's tip results in directional growth changes, forming a kink. This kink redirects the whisker's growth path, leading to the formation of an L-shaped structure that can cause further mechanical instability. These observations underscore how mechanical constraints, such as pressure from separators, influence lithium whisker growth, morphology, and stability.

High-surface-area Li morphology is highly affected by cell configuration and factors such as pressure and the presence of a separator. A recent work by LePage et al.[43] illustrates how mechanical constraints and external pressure can impact high-surface-area Li formation (Figure 9c). Operando microscopy shows that, without stack pressure, mossy Li grows unconstrained, resulting in the accumulation of inactive Li upon

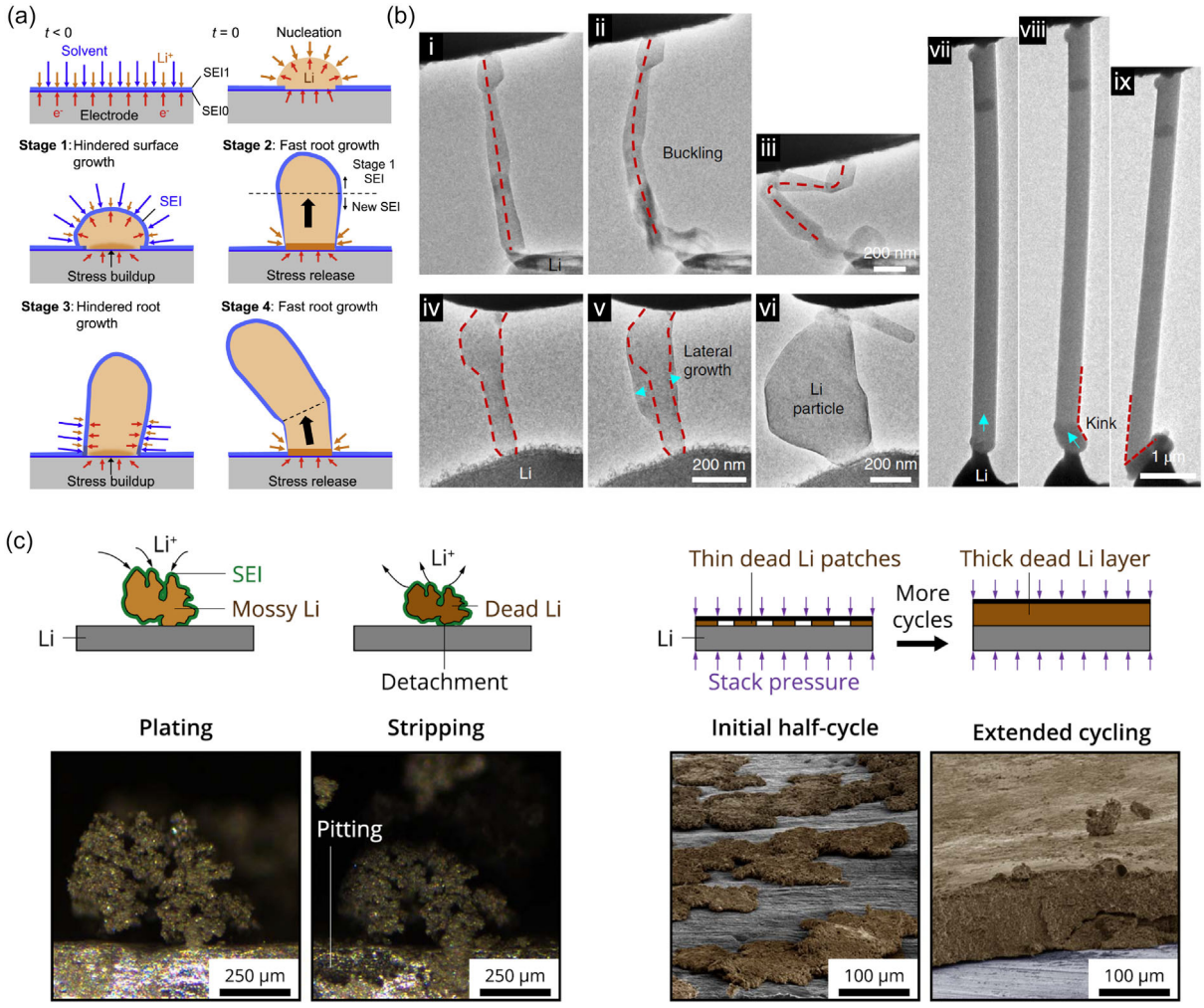

Figure 9. Impact of pressure on lithium growth: a) schematic illustration of the whisker-like Li growth process proposed by Li et al. (Stages 1–4): Stage 1 involves hindered surface growth due to stress buildup under the initial SEI layer, followed by Stage 2, where nucleation and fast root growth relieve stress, resulting in a new SEI formation. Stage 3 depicts hindered root growth, and Stage 4 concludes with lateral and particle-like growth as stress release mechanisms dominate.[42] b) Sequential TEM snapshots: (i–iii) Buckling of a Li whisker, (iv–vi) cessation of axial growth and subsequent lateral expansion forming a particle, and (vii–ix) kinking behavior of the whisker.[45] c) Optical and SEM images illustrate effect of pressure on mossy and inactive Li formation under unconstrained conditions, mossy Li forms during plating and transforms into inactive Li patches after stripping (left), and in constrained conditions, extended cycling leads to the compression of inactive Li patches into a thick, dense Li layer.[43] Reproduced with permission.[42] Copyright 2021, Elsevier, reproduced with permission.[42] Copyright 2019, Springer Nature, and reproduced with permission.[43] Copyright 2019, Electrochemical Society.

stripping. However, when constrained by stack pressure, Li forms a more flattened morphology. This demonstrates the significant effect of external pressure on Li growth, where increased compressive forces suppress vertical high-surface-area Li growth but induce the formation of inactive Li.

Pressure is one of the most crucial factors in determining the differences in performance between coin cells and pouch cells. Coin cells are commonly used for lab-scale testing,[46] while pouch cells provide more realistic insights into commercial battery performance.[47] However, due to significant pressure inhomogeneities in coin cells, their results often do not translate well to larger formats such as pouch cells. Soulen et al.[48] demonstrated that the geometry of the wave spring in coin cells creates an inhomogeneous pressure distribution, leading to non-uniform Li plating. Thicker, more dendritic deposits tend to form in the lower-pressure center, while denser, more compact plating occurs near the higher-pressure edges. Conversely, the pressure is more evenly distributed in pouch cells, resulting in more uniform Li plating and consistent cell performance (**Figure 10**a). This conclusion is supported by a detailed comparison of the Li plating morphology and thickness after the first cycle in both cell types, as shown in Figure 10b. The data highlights how pressure inhomogeneity in coin cells leads to a localized increase in current density, promoting non-uniform Li growth.

Liu et al.[49] expanded on the role of pressure at the pouch cell level, emphasizing that as the cell size increases, the role of pressure becomes even more important. Their study on large-area Li deposition in 350 Wh kg^{-1} pouch cells revealed that controlling external pressure is essential to reduce cell swelling and achieve uniform Li plating.

To translate the general "external-pressure" message into a concrete design rule, Efaw et al.[50] compared rigid constant-gap (CG)

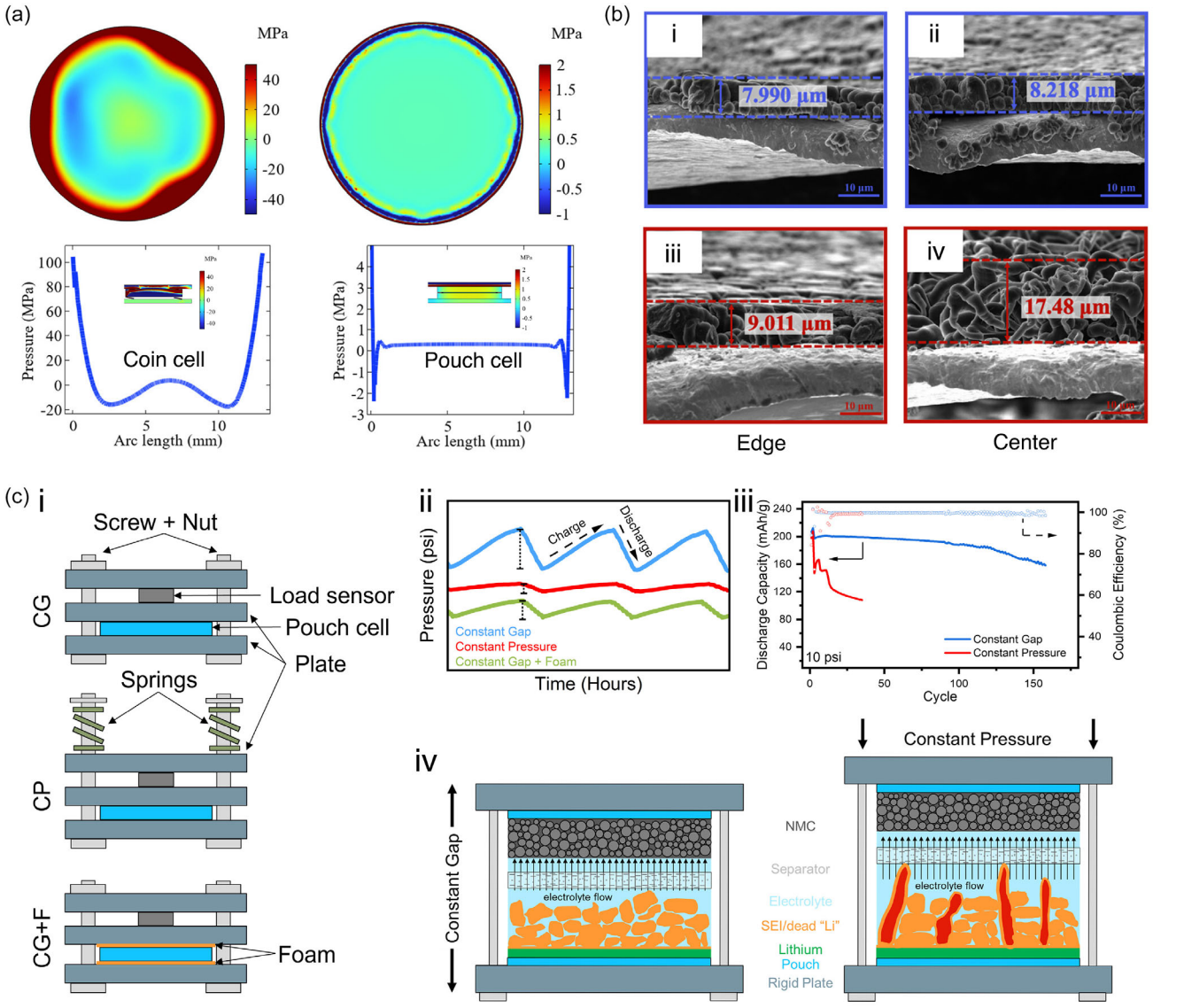

Figure 10. Impact of cell configuration on lithium deposition: a) pressure distribution simulations for coin cells (left) and pouch cells (right), illustrating the differences in pressure homogeneity across the arc length. Coin cells exhibit significant pressure variations, while pouch cells maintain uniform pressure distributions. b) Cross-sectional SEM images comparing Li deposition thickness at the edges and centers of coin cells i,ii) and pouch cells iii,iv).[48] c) Schematics of the three fixtures evaluated—CG, CP, and CG + foam (CG + F) i), operando stack-pressure traces under a 30 psi preload; CP pressure relaxes, whereas CG pressure self-ramps ii), discharge-capacity retention of CG versus CP cells under a 10 psi preload iii), and conceptual cartoons of Li deposition iv): dense plating under constant-gap confinement versus porous, electrolyte-starved growth under constant-pressure springs.[50] Reproduced with permission.[48] Copyright 2024, Electrochemical Society, and reproduced with permission.[50] Copyright 2019, Elsevier.

and spring-loaded constant-pressure (CP) frames in 100 mAh Li||NMC811 pouches operated with 3 g Ah^{-1} LHCE (Figure 10). At the same nominal 30 psi preload, the CG fixture sustained >250 cycles to 80% capacity, whereas the CP cell faded in <100 cycles (Figure 10c,iii). Operando load-cell traces revealed that CP springs accommodated early anode swelling, allowing the mean stack pressure to decrease, while the fixed CG gap enabled the pressure to self-ramp and densify the plated lithium. Finite-element simulations confirmed a nearly uniform compressive field under CG confinement, in contrast to edge-concentrated stress in the CP frame, hot spots that raising porous Li growth and local electrolyte starvation. Collectively, these findings establish constant-gap confinement as a mechanically adaptive and mass-efficient strategy for managing the large volume changes inherent to lean-electrolyte LMBs.

2.2.3. Influence of Temperature

Besides nucleation behavior and SEI formation, temperature is another crucial factor that affects high-surface-area Li growth.[51] high-surface-area Li growth patterns have been studied in experiments and computationally at various temperatures.[52] As shown in **Figure 11**, at low ambient temperatures of 0 and 20 °C, Li grows longer in the radial direction compared with temperatures of 40 and 50 °C, at which they are thicker in normalized width. This could be due to the chemical and structural changes in the

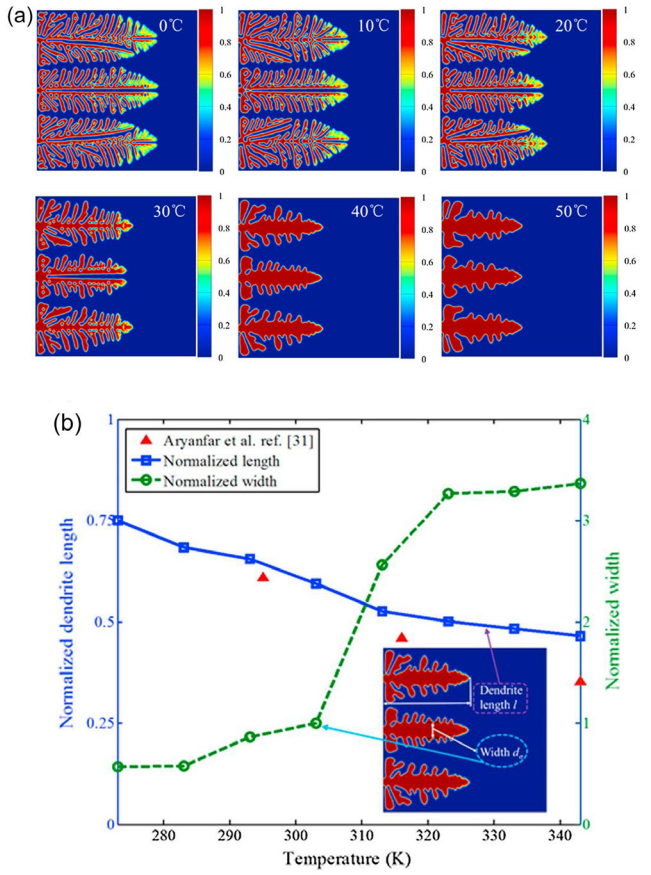

Figure 11. Impact of temperature on lithium growth: a) simulated high-surface-area Li morphologies at various ambient temperatures (0–50 °C) demonstrating how increasing temperature reduces high-surface-area Li length and promotes a thicker trunk, indicating temperature-driven suppression of lateral branching, and b) quantitative analysis showing normalized high-surface-area Li length and trunk width as functions of ambient temperature.[52] Reproduced with permission.[48] Copyright 2024, Elsevier.

SEI as well as differences in the mobility of Li-ions at different temperatures.

2.3. Stripping and Formation of Inactive Lithium

The Li stripping process, which in LMBs commonly follows a lithium deposition step, is as crucial as the latter. Li stripping refers to the removal of Li metal from the anode during the discharge of a LMB. Ideally, this process occurs uniformly across the anode surface, with all deposited Li being fully recovered. In practice, however, Li stripping is often inhomogeneous, leaving behind regions where Li is disconnected from the electrode. This leftover Li, encapsulated within a SEI layer, is referred to as inactive Li and represents a major contribution to reduced efficiency, capacity loss, and shortened cycle life of LMBs. The following sections will explore how inactive Li is formed as well as its impact on LMB performance.

Li et al.[53] found that during Li stripping, notches can form along the high-surface-area Li surface (**Figure 12**a). These notches are random locations where part of the Li whisker becomes completely pinched off, leaving isolated Li disconnected from the current collector, thereby contributing to the formation of inactive Li. The authors suggest that these notches emerge in areas where the SEI has a locally higher ionic conductivity, possibly caused by variations in SEI composition. These variations create pathways that favor faster Li dissolution in certain areas, leading to localized stripping and the eventual disconnection of parts of the whisker.

Werres et al.[54] explored the critical role of inhomogeneous Li stripping in the formation of inactive Li. Inhomogeneous stripping arises from interactions between Li and the SEI, which varies in structure and chemical composition across the anode surface. This variation leads to localized regions of Li dissolution, while other areas remain relatively untouched. As a result, portions of Li become electronically disconnected from the current collector. Over time, these disconnected Li deposits are encapsulated within an SEI shell, rendering them inactive. Based on cryo-TEM observations, a theoretical model was developed to show how certain regions of Li whiskers, particularly at kinks or bends, are more prone to the formation of inactive Li (Figure 12b). These kinked regions experience heterogeneous stripping due to irregular SEI coverage and local stress fields, which promote Li stripping in some areas while leaving others intact. This leads to Li being pinched off and trapped within the SEI, making it unable to participate in further electrochemical reactions. Moreover, the study demonstrates that higher current densities during Li stripping can mitigate the formation of inactive Li. At low current densities, the structure and localized variations of the SEI play a significant role in determining stripping behavior, resulting in greater heterogeneity and inactive Li formation. However, at higher current densities, the stripping process becomes more homogeneous, reducing the formation of inactive Li and enhancing battery efficiency.

A related study by Dutta et al.[55] further emphasizes the effect of discharge rate on Li stripping behavior. The researchers systematically examined Li stripping processes at varying discharge rates and identified distinct differences between slow and fast rates. At slower rates, the stripping process is highly heterogeneous, resulting in localized Li dissolution that exacerbates inactive Li formation. This inhomogeneity is driven by irregular SEI coverage and localized stress fields, which cause the isolation of Li particles within the SEI. In contrast, higher discharge rates promote more uniform Li stripping. Rapid dissolution occurs preferentially at high-curvature regions, such as the tips and edges of Li deposits, effectively reducing inhomogeneity (Figure 12c). This uniformity suppresses the formation of inactive Li and minimizes the accumulation of SEI products. Consequently, the volume expansion of the Li electrode is significantly reduced, improving cycle life. However, the study also highlights a threshold beyond which further increases in discharge rate result in diminishing performance due to kinetic limitations, particularly on Li^+ transport within the electrolyte and electrode interface. These findings underline the existence of an optimal discharge rate allowing uniform stripping and minimal inactive Li formation, thereby enhancing the performance and longevity of LMBs.

The formation of inactive Li is one of the major causes of battery failure, leading to capacity loss and reduced efficiency in LMBs, particularly under harsh conditions such as low temperatures, low

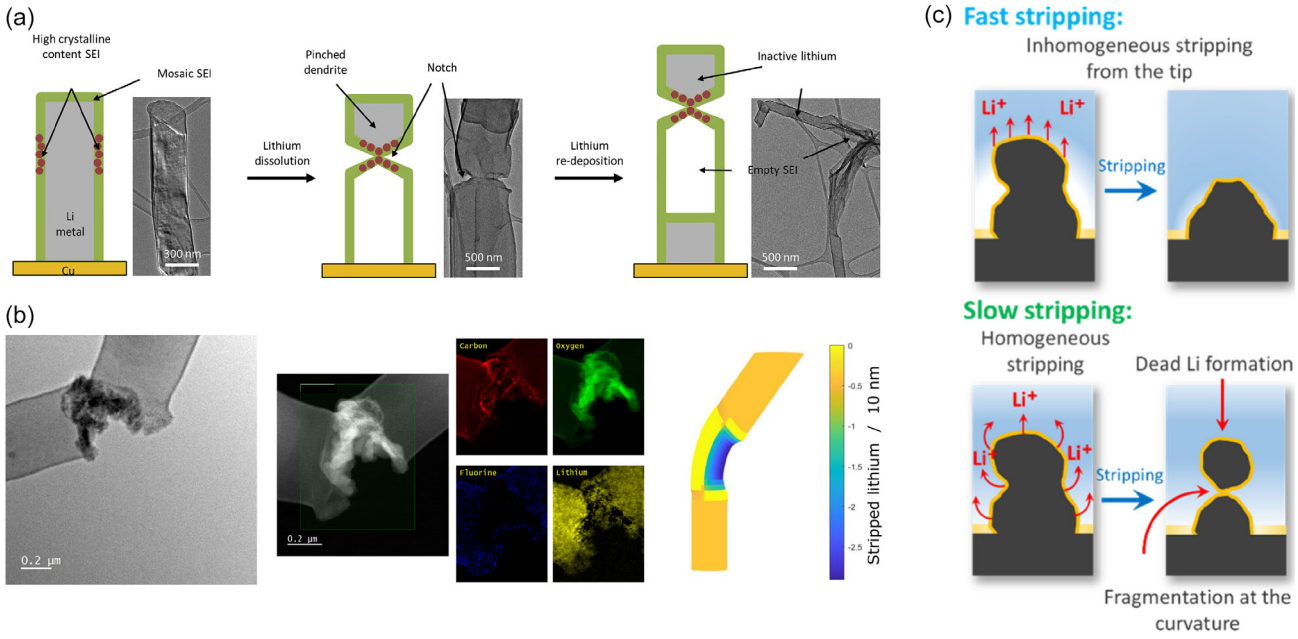

Figure 12. Lithium stripping mechanisms and formation of inactive lithium: a) sequential schematic and cryo-TEM images show the progression from an intact mosaic SEI to pinched dendrites and empty SEI shells, illustrating Li detachment at stress-concentrated regions;[53] b) elemental mapping (C, O, F, and Li) from cryo-EM analysis reveal distinct SEI structures at kinks or bends of Li whiskers, where stress and non-uniform dissolution promote inactive Li formation;[54] and c) schematic representations of stripping mechanisms under different conditions: fast stripping leads to inhomogeneous Li dissolution from the tip, resulting in inactive Li, whereas slow stripping promotes homogeneous dissolution but facilitates the accumulation of inactive Li at curvature points.[55] Reproduced with permission.[53] Copyright 2018, Elsevier, and reproduced with permission.[54] Copyright 2023, and reproduced with permission.[55] Copyright 2024, American Chemical Society.

pressures, or high current densities. Chengcheng et al.[56] systematically studied the correlation between CE and the formation of inactive lithium using various electrolytes. Their findings reveal that the structural morphology of deposited Li plays a critical role in determining the ability of active Li to maintain its structure during stripping.

In Li deposits with a whisker-like morphology and high tortuosity (**Figure 13**a), typically observed with commercial carbonate electrolytes, the microstructure is prone to losing electronic connections, resulting in significant inactive Li remaining within the SEI during the stripping process. In contrast, Li deposits with a denser, chunky morphology, and lower tortuosity (Figure 13b), as observed in high-concentration electrolytes, exhibit better structural integrity and maintain stronger contact with the current collector, leading to reduced unreacted metallic Li and higher CE. The ideal deposition morphology is a columnar microstructure with large, granular particles and minimal tortuosity (Figure 13c). This morphology minimizes unreacted Li_0 residue, reduces inactive Li formation, and maximizes battery performance.

Additionally, a homogeneous and elastic SEI is essential to ensure uniform Li^+ dissolution and accommodate volume changes during cycling. Chengcheng et al.[56] further revealed a clear relationship between CE and the ratio of SEI-bound Li^+ to inactive Li (Figure 13d). When CE falls below 95%, inactive Li becomes the dominant contributor to capacity loss, as tortuous, whisker-like deposits result in electrical isolation. Conversely, at CEs above 95%, SEI-bound Li^+ dominates, reflecting improved structural integrity and reduced inactive Li residue. This correlation highlights the importance of reducing tortuosity and promoting uniform Li deposition to enhance CE and minimize capacity losses. These features are critical for mitigating inactive Li formation and improving the overall performance and longevity of LMBs.

2.3.1. Pit Formation

Stripping of Li typically begins with the removal of the high-surface-area Li deposits formed on the surface of the anode during plating. However, since stripping is not homogeneous, the efficiency of the system is not 100%. As a result, once the high-surface-area Li deposits are stripped, any remaining Li required to balance the charge on the cathode side must be sourced from the bulk of the Li metal surface. Ideally, this process would occur uniformly across the electrode, but in practice, it often leaves behind voids and pits on the surface of the Li metal substrate. A key focus of recent research has been to understand the mechanisms behind this inhomogeneous stripping and the resulting pit formation.

Liu et al.[57] found that Li nucleation sites shifted to areas with pits formed during the Li stripping process. The relocation of nucleation sites is attributed to the higher local current density inside the pits compared to the unreacted Li anodes, as well as the electrochemical activation of these pits during the earlier dissolution process. As a result, these electrochemically activated regions become more favorable sites for subsequent Li nucleation.

In a related study, Sanchez et al.[14] used plane-view operando optical microscopy to examine the dynamic behavior of Li morphology deposited during the plating and stripping processes, correlating Li growth with changes in the voltage profile.

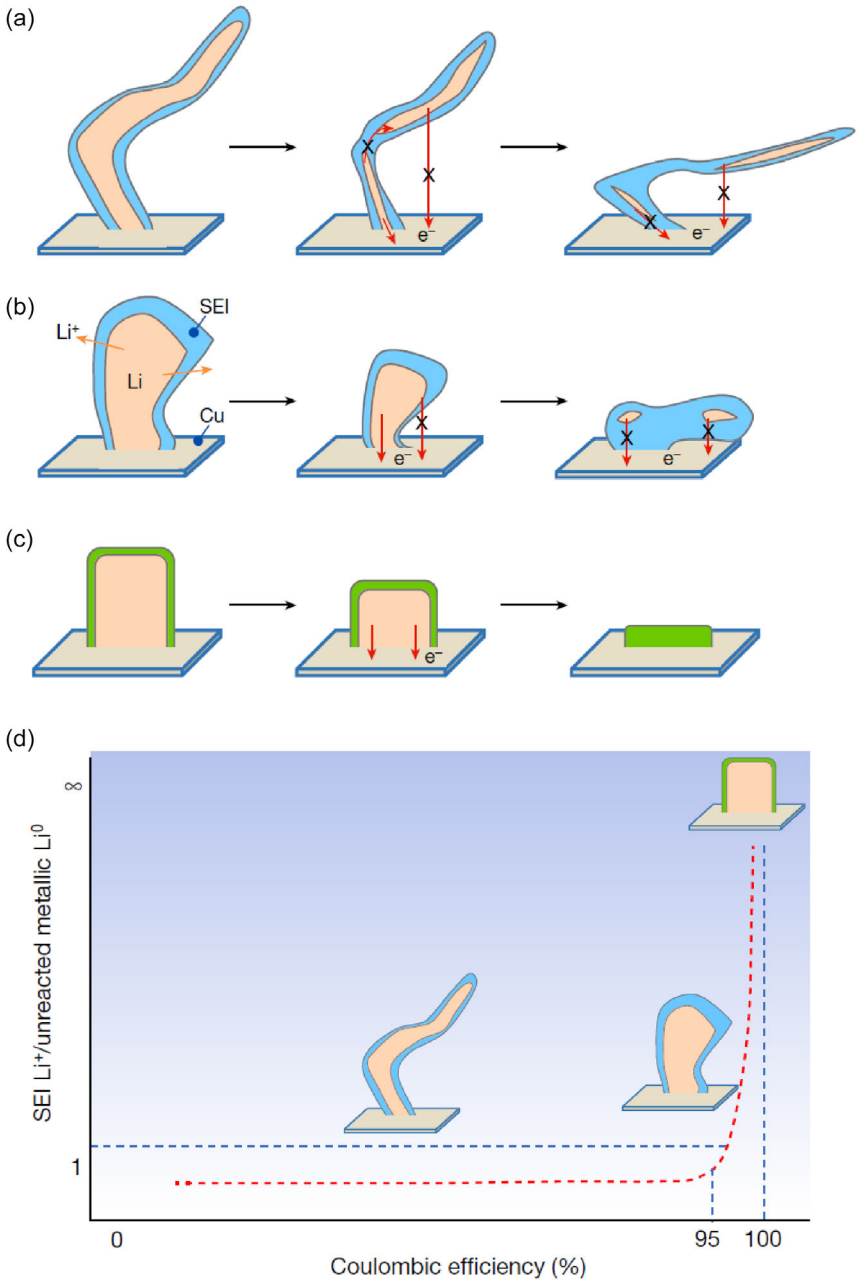

Figure 13. Impact of lithium deposited morphology on CE: schematic representations illustrating of: a) whisker-like Li deposits with high surface area and tortuosity are prone to losing electronic connections, leading to poor structural stability and the accumulation of large amounts of inactive Li within the SEI; b) Li deposits with larger granules and reduced tortuosity maintain more stable structural and electronic connections, resulting in smaller quantities of trapped Li at tortuous SEI edges; c) the ideal Li deposit should exhibit minimal tortuosity, a columnar microstructure with large granular sizes, and a homogeneous distribution of SEI components, facilitating efficient Li dissolution and reducing inactive Li formation; and d) the correlation between Li deposit morphology and the ratio of SEI Li^+ to unreacted metallic Li, highlighting the importance of uniform and stable Li morphology in achieving high CE.[56] Reproduced with permission.[56] Copyright 2019, Springer Nature.

Figure **14**a,i shows the working electrode, which initially has a planar surface with clearly visible cracks and microstructures. Once Li is deposited, it nucleates into a high-surface-area mossy morphology (Figure 14a,ii) which, when the current is reversed, shrinks and becomes electrically and/or physically isolated from the electrode surface, turning into inactive Li (Figure 14a,iii). Stripping of Li then shifts to the bulk of Li metal, leading to the emergence of voids and dips on the surface (Figure 14a,iv). The researchers also noted a distinct transition in the electrochemical dissolution site, identified by a second peak in the voltage profile. This peak is associated with the shift from high-surface-area Li stripping to the stripping of bulk Li. These formed pits on the surface of Li metal act as nucleation sites for new deposited Li in subsequent cycles, with high-surface-area Li forming exclusively inside pits during subsequent deposition (Figure 14a,v). The increasing surface area introduced by pit expansion

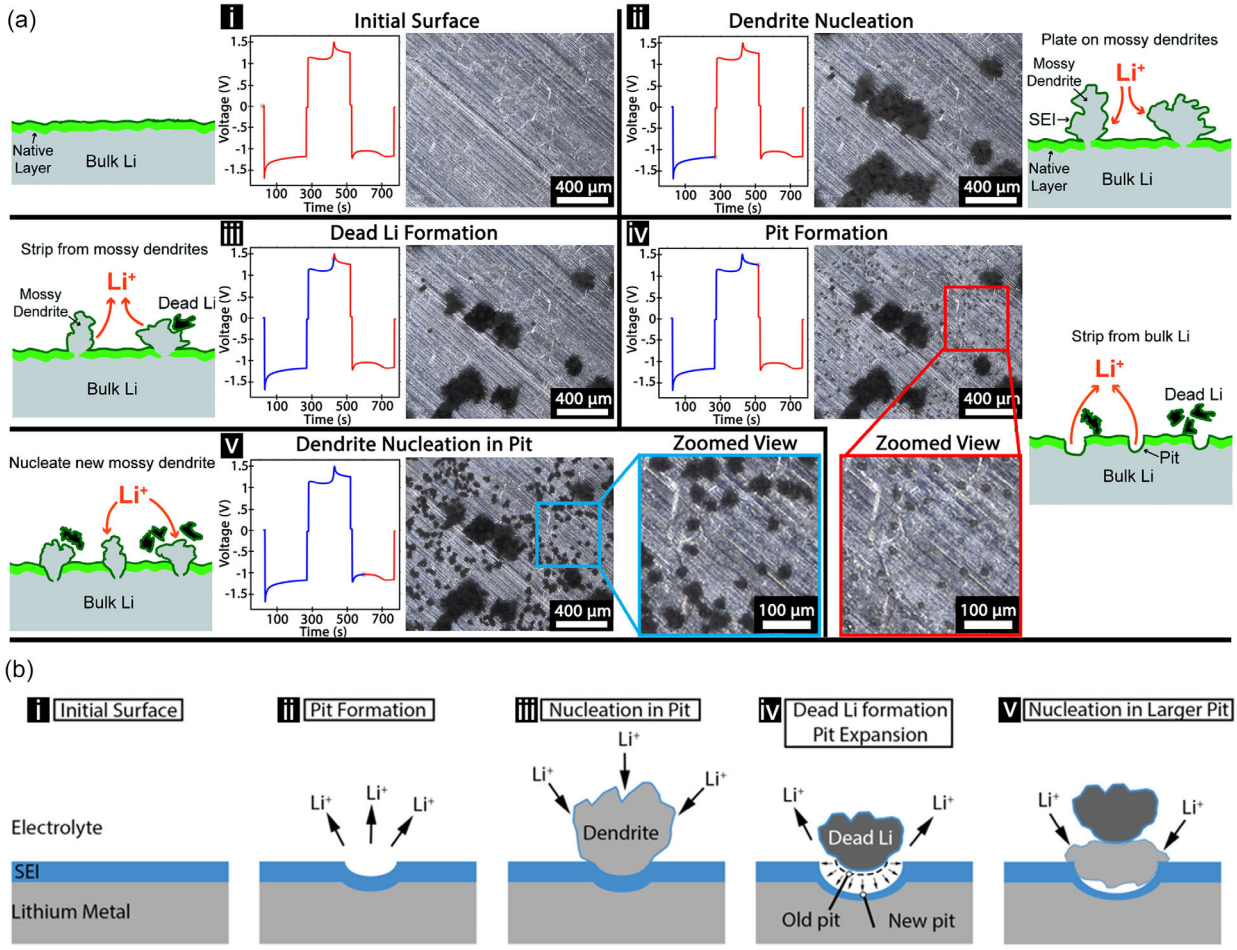

Figure 14. Evolution of lithium electrode surface morphology during cycling: a) schematic and operando video microscopy of correlation of surface morphology with voltage changes Li electrode during cycling (0.2 mAh cm^{-2} at 3 mA cm^{-2}): i) Native Li surface with a pristine SEI, ii) Li nucleation on mossy structures after plating, iii) Li stripping forming inactive Li encapsulated in the SEI, iv) pit formation and inactive Li accumulation at the end of stripping, and v) nucleation of mossy Li within expanded pits during subsequent plating (zoomed images show fine structural details of pits and high-surface-area Li formation). b) Schematic representation of Li electrode surface evolution during cycling, illustrating that Li deposition preferentially occurs within preformed pits.[14,58] Reproduced with permission.[58] Copyright 2017, Royal Society of Chemistry.

facilitates additional Li nucleation, which vertically displaces the inactive Li from the electrochemically active surface. Chen et al.[14,58] also schematized in a similar manner the progression of pit formation and evolution during lithium cycling (Figure 14b), emphasizing the importance of controlling pit formation during the early cycling stages. Precycling surface treatments, such as mechanical deformation or chemical modification, can play a critical role in preventing excessive pit formation and can significantly improve cycle life and CE.

Huang et al.[59] observed a similar behavior in their study of Li versus Cu AFLMBs, correlating the changes in Li nucleation, deposition, and dissolution with voltage fluctuations in their system. They investigated the mechanism of Li nucleation and deposition/dissolution on half cells using transmission X-ray and in situ optical microscopy, proposing the mechanism illustrated in **Figure 15**. They suggested that an initial energy barrier must be overcome by first forming nucleation sites on the Cu surface, resulting in a higher initial overpotential during Li deposition on Cu foil, similar to previous studies (Figure 15,i). These results, however, are challenged by more recent results from our team showing that the drop in overpotential in the first cycle was due to the extraction of Li from the counter electrode.[59] Thereafter, plating more Li results in high-surface-area Li appearing on the surface of Cu, which is accompanied by a decrease in overpotential (Figure 15,ii). During the following Li stripping from the Cu surface, a further increase in overpotential is observed due to the protrusion of the SEI layer and the growth of fresh Li on the surface (Figure 15,iii). Once this process is complete, the cell voltage suddenly increases because all available active Li are consumed, and only inactive Li are left on the Cu surface (Figure 15,iv). Meanwhile, on the Li electrode side, high-surface-area Li begins to grow on the roughened Li surface due to the non-uniform current distribution of the dissolution process. The plating and stripping of Li in the following cycles are generally similar to the first cycle in general, including fresh Li nucleation, SEI fracture, inactive Li formation, and growth on both sides (Figure 15,v). However, during the second cycle, an additional plateau with a potential similar to the deposition overpotential in the

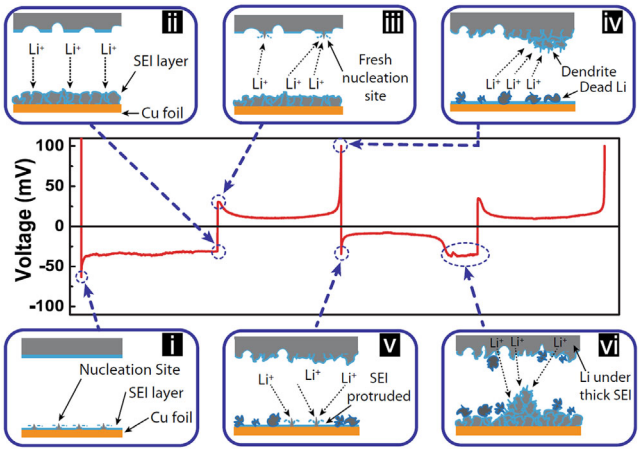

Figure 15. Lithium plating and stripping dynamics on copper foil: schematic representation of Li plating and stripping behavior on Cu foil in a half-cell, correlated with voltage changes: i) initial nucleation occurs under the SEI layer on the copper substrate, forming the first Li deposits; ii) Li plating continues, leading to localized deposition beneath the SEI, contributing to uneven surface morphology; iii) fresh nucleation sites form as deposition becomes less uniform, causing localized Li accumulation; iv) high-surface-area Li deposition and inactive Li form during stripping due to incomplete dissolution of deposited Li, leading to increased surface irregularities; v) SEI protrusion grows during extended cycling, further impacting Li-ion transport and deposition; and vi) Li becomes trapped beneath a thickened SEI layer, leading to inactive Li accumulation and reduced cycling efficiency.[59] Reproduced with permission.[59] Copyright 2021, Springer Nature.

first cycle was observed (Figure 15,vi). The authors claim that the first plateau results from Li being extracted from high-surface-area deposited Li, and the second plateau is due to Li being stripped from metallic Li. The lower potential in the galvanostatic curve indicates a more difficult Li extraction, resulting from a thicker SEI covering the bulk Li.

Pit formation on the Li metal surface during stripping is highly influenced by the applied current density and overpotential. As shown in **Figure 16**a of Zhang et al.'s study,[60] the formation of pits during stripping can be interpreted through a nucleation-like process, wherein higher overpotentials (arising from increased current densities) facilitate pit initiation by reducing the critical energy barrier and increasing the number of active sites. Although this behavior is often analyzed within the framework of classical nucleation theory, it should be noted that in this context, "nucleation" specifically refers to the initiation of voids (pits) during the dissolution of lithium, rather than the formation of a new solid phase. The study examined the effect of various current densities, ranging from 0.5 to 5 mA cm^{-2}, on pit formation using confocal laser scanning microscopy. At lower current densities, such as 0.5 mA cm^{-2}, pits were sparsely distributed and tended to nucleate at specific surface locations. The pits nucleated preferentially at low-energy barrier sites, leading to a non-uniform distribution. However, as the current density increased to 2 mA cm^{-2}, the nucleation density increased significantly, while the average pit radius decreased. By 5 mA cm^{-2}, the pit radius further decreased, and pits began to merge due to the higher number of nucleation sites formed at these elevated overpotentials. Importantly, the study found that the pits' depth and shape also evolved with current density. At low current densities, the pits grew with an asymmetrical shape, while higher current densities led to more uniform, circular pits. The correlation between overpotential and pit radius was inversely proportional, consistent with classical nucleation theory. The evolution of these pits is further illustrated in Figure 16b, which shows the stripping process over time. At low stripping capacities, newly formed pits have a wide and shallow shape. As the stripping progresses, these pits evolve into deeper, hemispherical depressions. The continuous decrease in pit radius and the transition to a more defined hemispherical shape with increasing current density creates additional surface area for subsequent high-surface-area growth during Li deposition.

Lu et al. observed similar trends in Li metal stripping and pit formation, despite working in different battery configurations.[61] In solid-state batteries, higher current densities lead to a greater number of smaller pits, which nucleate more readily due to the higher overpotential.

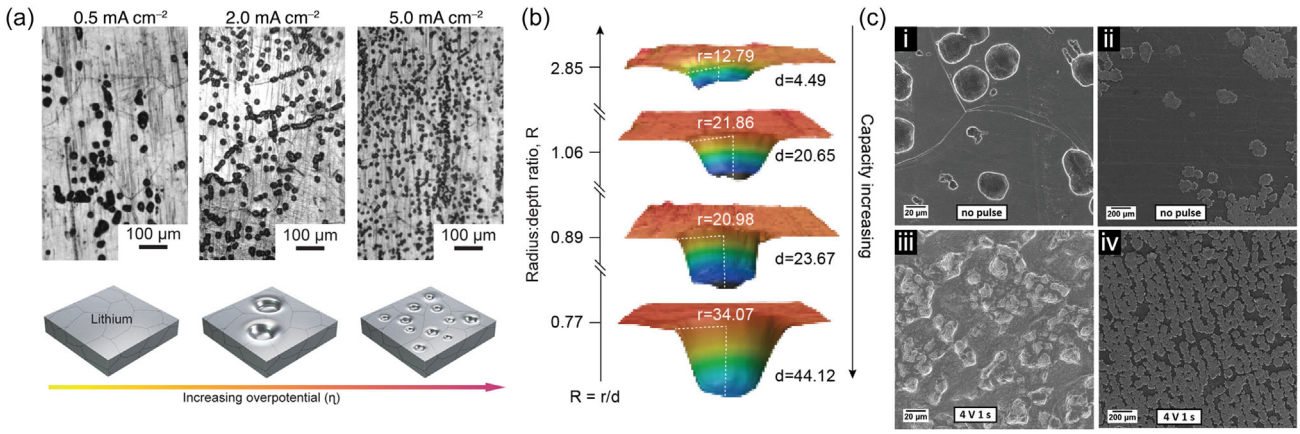

Figure 16. Impact of current density on pit formation: a) operando microscopy reveals increased pit density and smaller pit sizes with rising current density (0.5–5.0 mA cm^{-2}), b) 3D morphology analysis shows a transition from shallow to deeper pits with increasing stripping capacity,[60] and c) SEM images illustrate the influence of pulsed overpotential: i,ii) stripping and plating without pulsing result in uneven pits and non-uniform deposits and iii,iv) Stripping and plating with pulsed overpotential (4 V, 1 s) lead to uniform pits and evenly distributed deposits.[62] Reproduced with permission.[60] Copyright 2024, American Chemical Society, and reproduced with permission.[62] Copyright 2021, John Wiley and Sons.

Similar strategies based on his concept have been explored to improve battery performance. A prime example of this is the study conducted by Huang et al.[62] which focuses on the first-cycle oxidative generation of Li nucleation sites to stabilize Li metal electrodes. This approach shows how the formation of a large number of homogeneously distributed pits during the initial stripping step can significantly improve the deposition and stripping behavior in subsequent cycles (Figure 16). When a stripping pulse of 4 V for 1 s is applied before the first galvanostatic stripping step, a more homogeneous pit distribution is achieved, as shown in Figure 16,iii. This treatment leads to the formation of small, well-distributed pits compared to the uneven and sparse pit formation seen in Figure 16,i, where no pulse was applied. These uniformly distributed pits serve as preferential nucleation sites for Li deposition, resulting in a more controlled and stable Li growth. They also show that Li deposits more uniformly on electrodes treated with the stripping pulse, highlighting how initial surface activation can significantly enhance subsequent deposition behavior. This method creates a homogeneous electrochemically active surface, thereby improving the overall battery performance and extending cycle life by reducing the formation of inactive Li.

2.4. Evolving Inactive Lithium during Long-Term Cycling

After long-term cycling, LMBs often experience the gradual accumulation of inactive Li, forming a tortuous interphase on the surface of the Li metal anode. This layer of inactive Li can significantly impact battery performance by increasing resistance, limiting ion transport, and eventually leading to cell failure.

Kuan-Hung Chen et al.[58] demonstrated how this accumulation of inactive Li affects the voltage response of the battery. Initially, during the early stages of cycling, Li plating and stripping occur relatively uniformly, allowing for efficient ion transport. However, over repeated cycles, the buildup of inactive Li creates a complex, tortuous pathway (**Figure 17**a), increasing the cell resistance and altering its voltage profile.

Xia Cao et al.[63] investigated the role of electrolytes on the formation of inactive Li, showing that electrolyte composition plays a crucial role in the chemical and structural properties of the SEI. As illustrated in Figure 17b, a more homogeneous and robust SEI, achieved using fluorinated orthoformate-based electrolytes, can significantly minimize inactive Li formation. By forming a monolithic SEI, these electrolytes suppress the continuous side reactions between Li and the electrolyte, thus reducing the buildup of inactive Li and maintaining a more stable battery performance over extended cycling.

More recently, Chen-Xi Bi et al.[64] visualized the evolution of the Li metal surface at different states of charge and discharge using SEM images at the end of cycling, as shown in Figure 17c. Their results reveal that new Li is deposited on top of the accumulated inactive Li with each cycle rather than integrating with the bulk Li metal. This creates a layered structure where the inactive Li becomes more prominent, and fresh Li continuously forms on top. Over time, this process leads to a thickened, nonconductive layer that exacerbates the challenges of ion transport, contributing to the rapid degradation of battery performance.

The formation of inactive Li on the anode surface is a critical issue that significantly impacts the long-term performance of LMBs. As shown by the previously discussed studies,[58,63,64] the gradual accumulation of inactive Li leads to increased resistance, reduced efficiency, and eventual cell failure. Given its substantial influence on battery performance, it is crucial to develop methods to accurately quantify the amount of inactive Li that forms during cycling. The quantification of inactive Li also enables the evaluation of strategies aiming to minimize its formation and extend cycle life. The progressive accumulation of inactive

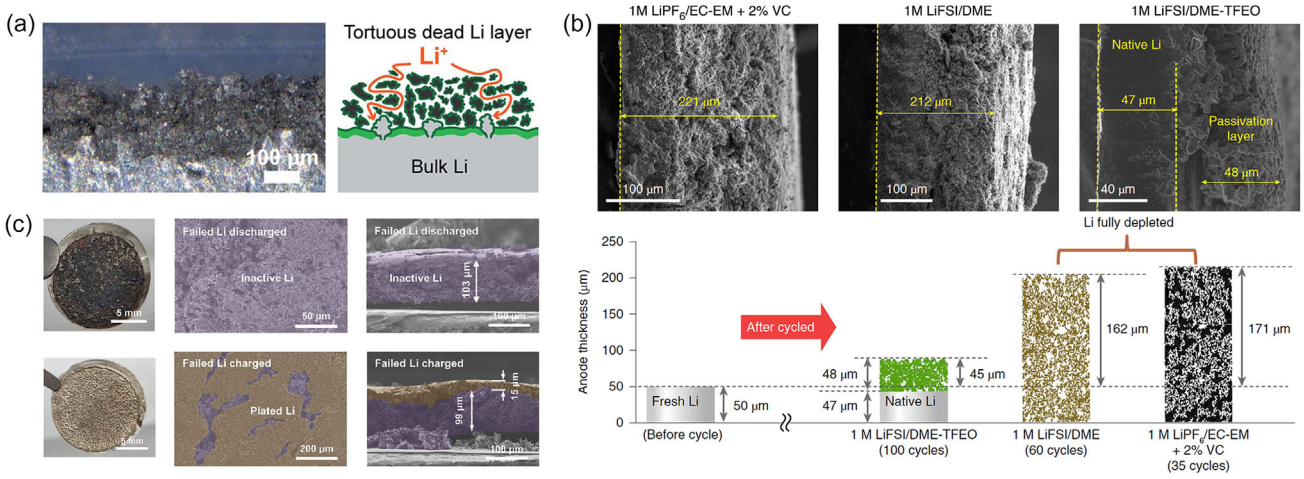

Figure 17. Evolution of inactive lithium formation during extended cycling: a) formation of a tortuous, inactive Li layer due to incomplete stripping and continuous SEI formation, as revealed by microscopy;[58] b) cross-sectional SEM images illustrate the effect of different electrolytes on anode morphology after cycling;[63] and c) visual and SEM images of cycled anodes show the accumulation of inactive Li in discharged cells and the formation of layered structures with plated Li in charged cells. This illustrates how fresh Li deposits on top of inactive Li layers, exacerbating challenges in ion transport and contributing to the thickened, non-conductive interphase.[64] Reproduced with permission.[58] Copyright 2017, Royal Society of Chemistry, reproduced with permission.[63] Copyright 2019, Springer Nature, and reproduced with permission.[64] Copyright 2024, John Wiley and Sons.

lithium during extended cycling is further examined in the following sections, with a focus on its quantification and mechanistic interpretation. We will explore the methods and techniques currently used to quantify inactive Li on the surface of Li metal and provide insights into how this knowledge can drive the development of more robust and reliable LMBs.

3. Quantification of Inactive Lithium

The precise measurement of inactive Li is pivotal for understanding its impact on battery degradation. Over the years, researchers have implemented various methods (from ex situ to operando) to measure the quantity, distribution, and composition of inactive Li in Li metal anodes.[65,66] These approaches incorporate advanced diagnostic tools such as XRD,[67–71] operando neutron depth profiling (NDP),[72,73] titration-based techniques,[74–102] NMR spectroscopy,[93,98,101,103–112] fluorescence probing,[113–115] and simulation or physics-based models.[116–118] In the following subsections, we focus on two leading methods: titration-based approaches and NMR spectroscopy. We discuss the underlying principles of each technique, alongside representative applications, to illustrate their capabilities in detecting inactive Li. In addition, we summarize other noteworthy methods and provide a holistic perspective on the current state of quantification strategies for inactive Li in Li metal anodes.

3.1. Titration-Based Techniques for Quantifying Inactive Lithium

TGC is increasingly used as a sensitive and adaptable method for measuring inactive lithium in batteries. The basis of this technique is the reaction of the electrode with a titrant, which produces gas. The evolved gas is then analyzed to determine the quantity and form of lithium in the electrode.

Fang et al.[74] were the first to develop and refined the TGC approach for accurately quantifying inactive Li. As shown in **Figure 18**a, in this method, Li reacts with water to form hydrogen gas (H_2), which is then detected by gas chromatography. Because SEI components such as Li_2CO_3 and LiF do not produce gases under these reaction conditions, the TGC technique can selectively quantify metallic Li. They demonstrated that inactive Li primarily contributes to capacity loss in systems with CE below 95%, whereas SEI-related losses dominate in higher-CE systems (Figure 18b).

Despite its advantages, TGC has been used mainly for Li||Cu or AFLMBs configurations, where inactive Li remaining on the inactive current collector can be measured directly. However, TGC alone cannot distinguish between "active" and "inactive" Li deposited on Li metal anodes in realistic cells. To address this limitation, Deng et al.[91] integrated TGC with ICP-OES. As illustrated in Figure 18c, their hybrid method selectively dissolves active metallic Li using biphenyl in tetrahydrofuran (THF), thereby isolating encapsulated Li. Subsequently, water is added to

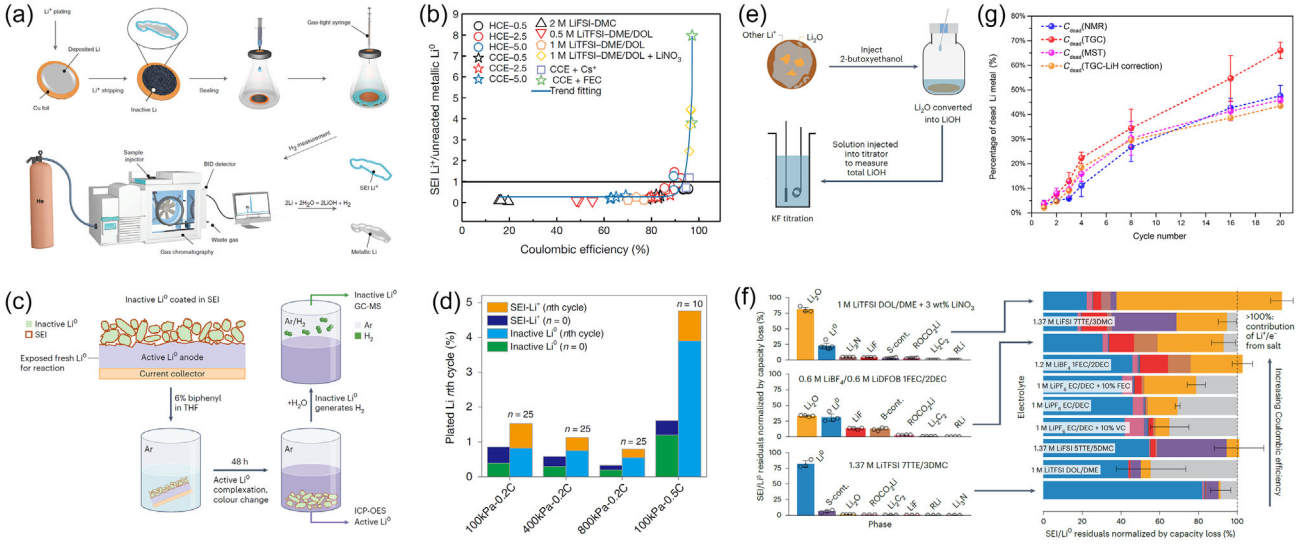

Figure 18. Titration-based techniques for quantifying inactive lithium: a) schematic representation of TGC, highlighting how inactive Li reacts with water to form hydrogen gas (H_2), selectively quantifying Li while excluding SEI components like Li_2CO_3 and LiF; b) CE versus SEI Li^+/unreacted Li ratio for different electrolytes; high-concentration electrolyte (HCE; 4 M liFSI + 2 M liTFSI in DME), commercial carbonate electrolyte (CCE; 1 M $LiPF_6$ in EC/EMC) at three stripping rates (0.5, 2.5, and 5.0 mA cm^{-2}; all plating at 0.5 mA cm^{-2} for 2 h);[74] c) A hybrid method combining TGC and ICP-OES to distinguish active metallic Li from inactive Li: active Li is dissolved in biphenyl/THF, leaving encapsulated Li for subsequent reaction with water to quantify H_2 production;[139] d) Effect of stack pressure and cycling conditions on Li morphology, showing reduced Li loss at higher pressures due to SEI stabilization and suppressed high-surface-area Li growth;[91] e) alcohol-based titration method converting Li_2O into LiOH, quantified via Karl Fischer titration, revealing oxygenated SEI phases like Li_2O as dominant contributors in high-CE systems; f) Comparison of SEI/Li^+ residues normalized by capacity loss across various electrolytes;[92] and g) Quantification of inactive Li evolution over cycling using complementary techniques (TGC, MST, and NMR), emphasizing their strengths and limitations in characterizing inactive Li species.[101] Reproduced with permission.[74] Copyright 2019, reproduced with permission.[91] Copyright 2022, reproduced with permission.[92] Copyright 2024 and reproduced with permission.[139] Copyright 2022, Springer Nature, and reproduced with permission.[101] Copyright 2025, American Association for the Advancement of Science.

dissolve the SEI and react with the isolated inactive Li, producing H_2 for TGC quantification. Meanwhile, ICP-OES measures the dissolved active Li, thus providing a more comprehensive assessment of Li reversibility and loss mechanisms. Their results demonstrate that increasing stack pressure (from 100 kPa to 800 kPa) significantly improves the plating/stripping reversibility, reducing cracking of the SEI and limiting the agglomeration of inactive Li (Figure 18d). At higher pressures, the formation of compact and uniform Li deposits minimizes voids and enhances electron and ion transport, while lower pressures lead to high-surface-area Li growth and higher rates of irreversible Li accumulation. The authors also used the same methodology to investigate the impact of current density. Their quantitative analysis showed that at higher charge/discharge rates (0.5C), faster Li deposition increases the inhomogeneity, promoting high-surface-area Li growth and cracking of the SEI, which accelerates the accumulation of inactive Li and diminishes reversibility. Although this hybrid approach extends the capabilities of TGC, it still relies on gas evolution, which excludes certain SEI phases (e.g., Li_2O) that do not generate gaseous byproducts.

To address the limitation in quantifying non-gas-producing compounds, Hobold et al.[92] developed an innovative alcohol-based titration method (Figure 18e). This method involves converting Li_2O to LiOH using 2-butoxyethanol, followed by quantification through Karl Fischer titration. Unlike traditional titration techniques, which often miss Li_2O due to its inert nature, this approach specifically targets Li_2O, offering a clearer picture of its prevalence in the SEI. Their results, illustrated in Figure 18f, reveal that in electrolytes which typically generate a desirable SEI and thus higher CEs, Li_2O emerges as a dominant SEI phase, correlating strongly with CE. For instance, electrolytes such as 1 M $LiPF_6$ in EC/EMC with 10% FEC yielded SEIs where Li_2O constituted 26.4% of the total mass, compared to only 6.7% in systems without fluorinated additives. Additionally, electrolytes such as 1 M LiTFSI in DOL/DME with $LiNO_3$ showed a dramatic Li_2O proportion of 80.8%, reinforcing its critical role in achieving near-complete Li utilization. These findings reveal that the prevalence of Li_2O is not exclusive to fluorinated electrolytes but is also observed in systems optimized for enhanced interfacial stability. This study highlights the pivotal role of Li_2O in stabilizing the SEI by improving Li^+ transport, mitigating interfacial resistance, and suppressing side reactions. By challenging the conventional focus on LiF, the findings emphasize the importance of oxygenated SEI phases, particularly Li_2O, in achieving efficient and stable cycling in LMBs. This innovative quantification method not only deepens our understanding of SEI chemistry but also paves the way for electrolyte designs that prioritize oxygen-rich phases for improved battery performance.

Recent studies have further utilized titration-based techniques to explore how temperature, pressure, and electrolyte affect the formation of inactive Li. For example, Zhang et al.[80] investigated the evolution of inactive Li at different temperatures, finding that high temperatures reduce inactive Li by promoting more compact Li deposition. In contrast, lower temperatures favor dendritic growth and lead to greater accumulation of inactive Li. Similarly, Lu et al.[78] demonstrated how localized high-concentration electrolytes (LHCE) reduce inactive Li formation by correlating Li deposition porosity with corrosion rates, measured via TGC over prolonged cycling. In addition, Gervillié–Mouravieff et al.[89] showed that carefully optimized stack pressures suppress dendritic growth and mitigate inactive Li accumulation, as confirmed by TGC measurements. Titration data were employed to validate mathematical models predicting Li loss and SEI growth under diverse cycling conditions, thereby linking experimental results to theoretical insights.

Although TGC delivers high sensitivity and quantitative accuracy, it remains limited by ex situ measurement requirements and the difficulty of differentiating overlapping gas signals. A key assumption in TGC is that only inactive Li reacts with the water to yield H_2. However, LiH may also react with water to produce H_2, potentially biasing the quantification of inactive Li. To address this limitation, mass spectrometry titration (MST) has been introduced.[85,95,99–101] By using deuterium oxide (D_2O) instead of H_2O, MST distinguishes H_2 from HD signals, enabling precise quantification of LiH alongside metallic Li. This development further refines TGC's application for characterizing inactive Li and provides critical insights into the interplay between LiH, SEI components, and inactive Li during cycling. While several studies have investigated the impact of LiH on battery performance, the findings have often been inconsistent and, in some cases, contradictory. The formation and accumulation of LiH can alter the properties of the SEI, potentially affecting both capacity retention and cycling efficiency. Nonetheless, its exact role in performance degradation and long-term battery reliability remains debatable.[85,99,100,119–122]

Since TGC generally attributes all hydrogen gas production to Li, LiH-generated hydrogen can lead to overestimations of inactive Li. Thus, to investigate the impact of LiH on the accuracy of TGC measurements, Xiang et al.[101] compared MST, TGC, and NMR data and found that TGC indeed overestimates inactive Li in systems with substantial LiH (Figure 18g). Employing MST with D_2O titrant, they validated NMR-based measurements of inactive Li, and MST-corrected TGC values aligned closely with the NMR benchmarks.

Owing to the challenges of achieving high CE in conventional coin cells, existing investigations of LiH have primarily focused on low-CE systems (<99%). The relatively high levels of free hydrogen in these electrolytes can promote significant LiH formation, increasing further by excess Li and electrolyte volumes. By contrast, recent electrolyte concepts such as HCEs, LHCEs or all-fluorinated electrolytes (AFEs) typically exhibit higher CEs (>99%) and thus contain less hydrogen overall, potentially leading to lower LiH formation. Likewise, practical pouch cells operate with a lower ratio of electrolyte to electrode materials, further reducing conditions that favor LiH formation. Recently, Liu et al.[99] performed a thorough *postmortem* analysis of Ah-level (450 Wh kg^{-1}) NCM811||Cu pouch cells employing AFE and LHCE electrolytes with high CE values (>99%). Although these two cell types exhibited distinct failure modes, i.e., "sudden death" dominated by inactive Li and "gradual decay" influenced by SEI buildup, the capacity loss attributable to LiH remained below 2.4% at 20% overall capacity fade, representing less than 12% of the total inactive Li (**Figure 19**a). These observations highlight that, under practical cell conditions, LiH generally plays a secondary role compared to inactive Li and SEI growth.

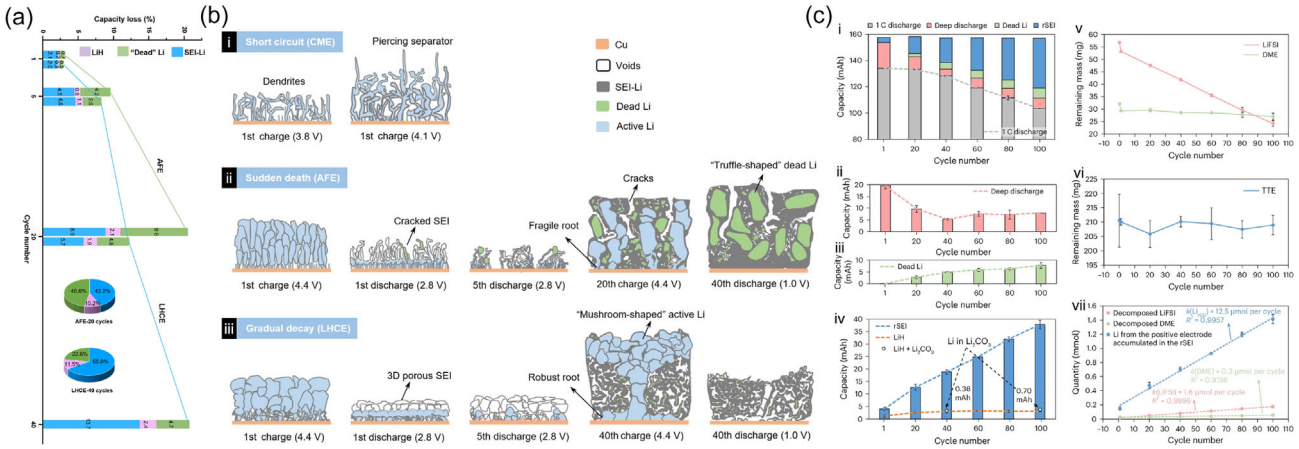

Figure 19. Failure modes and inactive lithium accumulation: a) quantitative breakdown of capacity loss into key inactive Li components, including SEI-Li, dead (inactive) Li, and LiH, over 1, 5, 20, and 40 cycles for cells with AFE and LHCE electrolytes and b) morphological evolution and failure modes across different electrolytes: i) short circuit (dendritic growth pierces the separator, causing short circuits during early cycling); ii) sudden death (inactive Li accumulates rapidly due to brittle SEI cracking and dendrite formation, leading to capacity loss); and iii) gradual decay (a 3D porous SEI structure and robust root formation suppress dendritic growth, resulting in slower capacity fade and gradual failure).[99] c) Quantitative mass balance of lithium and electrolyte degradation in Cu||NMC811 pouch cells: i) distribution of discharge capacity among active Li, inactive (dead) Li and rSEI determined by deep-discharge T-DEMS; ii) evolution of deep-discharge capacity; iii) equivalent Li in "dead" Li; and iv) Li trapped in rSEI over 0–100 cycles. Masses of residual LiFSI salt (v) and DME solvent (vi) tracked by extraction–gas & ion chromatography, highlighting preferential LiFSI depletion, and vii) linear fits give consumption rates k(LiFSI) = 1.6 μmol cycle^{-1} and k(DME) = 0.3 μmol cycle^{-1} versus Li sequestered in rSEI (12.5 μmol cycle^{-1}), confirming anion-driven active-Li loss.[123] Reproduced with permission.[123] Copyright 2025, Springer Nature.

Additionally, as illustrated in Figure 19b, the authors proposed three distinct failure mechanisms:[99] 1) short circuit (dendrites breach the separator, causing an internal short circuit). MST confirms that dendrite growth is accelerated in low-CE systems with elevated LiH and inactive Li formation. 2) Sudden death: Rapid accumulation of inactive Li leads to abrupt capacity loss. MST shows that while LiH is present, high-CE systems suffer primarily from inactive Li accumulation. Regulating stack pressure and electrolyte composition mitigates this failure mode by reducing SEI fracturing. 3) Gradual decay: Progressive SEI growth causes an increase in resistance and a gradual capacity decline in capacity. MST analysis suggests that Li_2O and organic SEI species dominate the inactive Li in high-CE cells. Although these failure modes are well-characterized in pouch cells, operating conditions (including current rate, temperature, and mechanical pressure) can also influence performance and potentially shift the dominant mechanism of failure.

Complementing the morphology-driven failure map proposed by Liu et al.[99] Wang et al.[123] turn the spotlight to the chemical side of inventory loss. Using a combined deep-discharge titration-DEMS and extraction gas and ion-chromatography protocol on lean-electrolyte (2.1 g Ah^{-1}), LiFSI-rich Cu||NMC811 pouch cells, they construct a full mass-balance for metallic Li, LiFSI salt and ether solvents. Their analysis reveals that LiFSI anion reduction proceeds at ≈1.6 μmol cycle^{-1}, five times faster than solvent decomposition, and immobilizes ≈12.5 μmol of Li cycle^{-1} in an anion-derived rSEI, leaving only a minor share of electronically isolated "dead" Li (Figure 19c). By demonstrating that salt depletion, rather than metallic isolation, becomes the dominant sink for active Li under high-CE, electrolyte-lean conditions, they provide the chemical rationale for the "gradual-decay" pathway and underscore the necessity of controlling anion reactivity alongside deposition morphology when designing long-life pouch cells.

In several studies, MST was applied to investigate the mechanisms of LiH formation, its temperature-dependent behavior,[100] and its variation across different electrolyte types,[98,95] providing a broader understanding of inactive Li evolution in LMBs. While MST is a destructive technique and not suitable for real-time, in situ, or operando analysis, it remains a powerful tool for post-mortem quantification of inactive lithium species. Combining MST with advanced in situ and operando methods can offer a more comprehensive understanding of the formation and evolution of inactive lithium under realistic operating conditions. Such integrated approaches are crucial for optimizing electrolyte formulations and developing robust interfacial engineering strategies aimed at maximizing the cycle life and performance of future LMBs.

3.2. Nuclear Magnetic Resonance Spectroscopy

Solid state NMR spectroscopy, as a versatile and noninvasive technique, can offer valuable insights into reversible Li^+, high-surface-area deposited Li, inactive Li, and SEI species in various battery configurations and technologies. NMR distinguishes between metallic lithium and diamagnetic Li^+ ions because the interactions between nuclear spins and conduction electrons in metals give rise to the Knight shift, shifting the metallic Li signal to much higher resonance frequencies.[108] This allows for measurements in static mode, i.e., without magic angle spinning (MAS), enabling in situ and *operando* NMR measurements (**Figure 20**a), as well as ex situ and *postmortem* studies. In addition, the resonance frequency of NMR signals also depends on the orientation

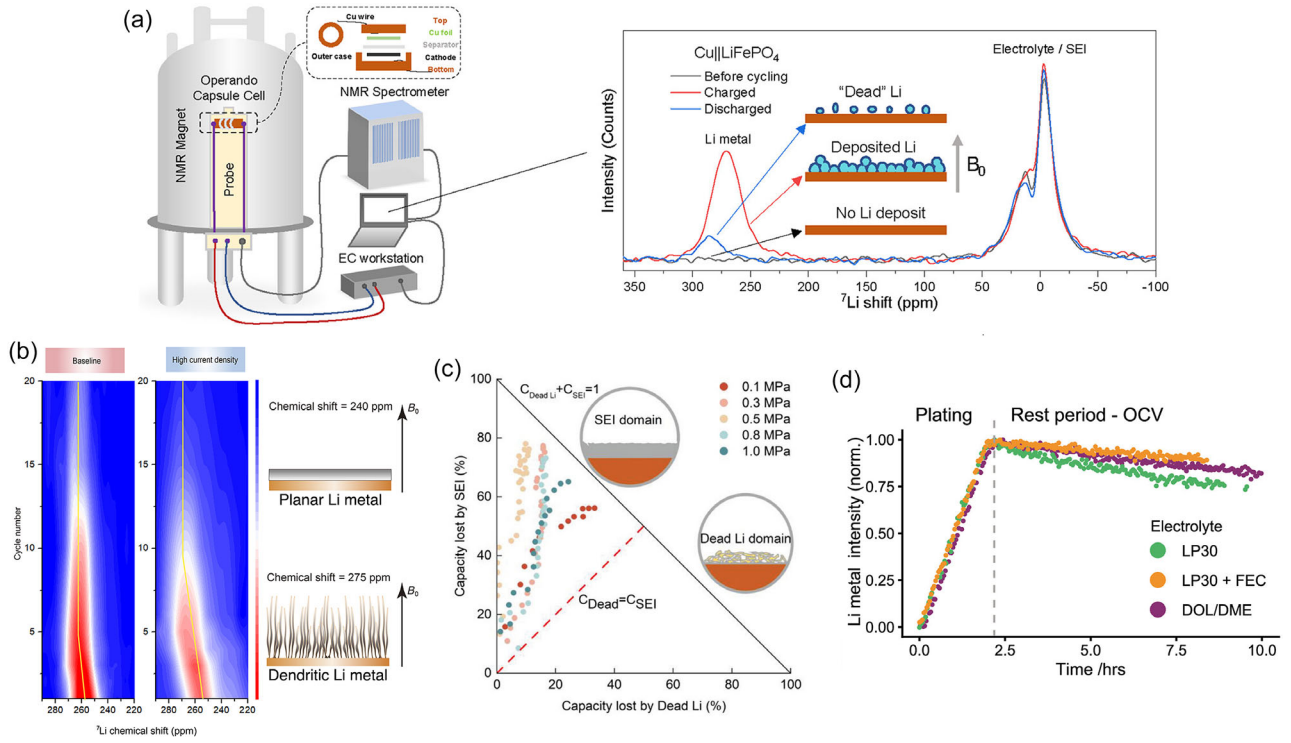

Figure 20. NMR spectroscopy for quantifying inactive lithium: a) schematic of the operando NMR setup illustrating how Li metal, SEI, and dead (inactive) Li are monitored in real-time during cycling in a Cu||$LiFePO_4$ cell; the corresponding spectra highlight distinct resonances for deposited Li, inactive Li, and SEI components.[110] b) operando NMR spectra show the chemical shift evolution during cycling, differentiating between planar Li and dendritic Li structures under varying current densities.[101] c) Quantitative analysis of SEI and inactive Li contributions to capacity loss at various stack pressures reveals a balance point at 0.5 MPa for minimized inactive Li formation.[111] d) Time-resolved NMR intensity measurements at OCV demonstrate the stability of Li deposits in different electrolytes (LP30, LP30 + FEC, and DOL/DME), emphasizing the role of SEI and electrolyte composition in preserving Li during rest periods.[108] Reproduced with permission.[108] Copyright 2020 and reproduced with permission.[110] Copyright 2022, American Chemical Society, reproduced with permission.[101] Copyright 2025, American Association for the Advancement of Science, and reproduced with permission.[111] Copyright 2024, John Wiley and Sons.

of the sample relative to the external magnetic field. This phenomenon, attributed to the Bulk Magnetic Susceptibility (BMS) effects, allows for differentiating between the Li metal foil and the microstructures/dendrites deposited perpendicularly on its surface.[124] Going even further, NMR can reveal the microstructure and the morphology of the deposited Li, since rougher whisker-like and dendritic Li deposits appear at chemical shifts higher than those of mossy deposits (Figure 20b).[101,104]

While NMR is known as a quantitative tool, it must be noted that radiofrequency pulses have a limited penetration depth in metals. This issue, known as skin depth, depends on the nuclei and is typically between 12 and 15 μm for ^{7}Li at relatively low magnetic fields ($B_0 \leq 7$ T).[104,108,124] Fortunately, this depth is longer than the size of deposited microstructures/dendrites, allowing for reliable detection and quantitative analysis of these species. This makes NMR a powerful tool for quantifying inactive Li and investigating parameters that affect irreversible capacity losses and dendrite growth. For instance, comparing the NMR spectra recorded before and after electrochemical cycling reveals the residual metallic Li signal, indicative of inactive Li. Extending this to further cycles, the accumulation of inactive Li on the current collector can be demonstrated. This method has been widely adopted to investigate the impact of electrolyte additives on inactive Li formation and the morphology/homogeneity of the Li deposits.[104,108,124]

The contribution of the SEI and inactive Li to the capacity loss can be achieved from the quantitative NMR results and the electrochemical data, particularly CE.[104,108,124] By following these contributions at each cycle, the dominant failure mode and its evolution can be studied. This approach was presented in the work of Xiang et al.[101] who depicted that the failure mechanism in LFP-based AFLMBs is dominated by inactive Li metal at high stripping current densities, while it is SEI-dominated when electrolyte additives are used. Applying a similar method, Lin et al.[111] studied the impact of stack pressure on the formation of inactive Li and its morphology, demonstrating that a medium pressure of 0.5 MPa results in a minimal quantity of inactive Li (Figure 20c). A similar work by Wang et al.[106] reported a decrease in inactive Li formation when using high-entropy electrolytes, leading to their higher CE. The same group also investigated the contributions of SEI and inactive Li to capacity loss across different electrolyte concentrations.[110] They observed that despite the higher reversible capacity obtained with higher electrolyte molarities, the metallic ^{7}Li NMR signals appear at higher chemical shifts. This was attributed to the lower Li deposit coverage, as the proximity of the Li deposits to the current collector affects their chemical shift. Thus, they proposed to replace the regular current collectors with nanostructured Cu and observed a noticeable increase in the deposition coverage and the microstructure morphology,

allowing the long cycle life of the AFLMBs.[110] Finally, Kwon et al.[109] investigated the cathode effect by comparing two AFLMBs with LFP and NMC electrodes. In this study, the in situ measurements were performed in the pouch cell configuration, showing the versatility of NMR. It was demonstrated that while the Li deposits in LFP cells are dense and highly reversible, the NMC cathodes operating at higher voltage form a high amount of inactive Li, with deposits having a porous nature. Interestingly, in the case of LFP cells, the amount of inactive Li formed during each cycle shows negative values for some individual cycles. This observation was attributed to the revival of inactive Li, pointing out the potential of in situ NMR for future studies on reactivating inactive Li in LIBs.

In situ and operando NMR methods have also been recently applied to solid-state batteries, particularly to investigate the capacity loss and failure modes among various solid electrolytes. In this case, NMR differentiates between the inactive Li formed on the Cu current collector and the high-surface-area Li grown inside the cracks of the solid electrolyte, with the latter appearing at a higher chemical shift.[107] The authors also demonstrated that, in the case of solid electrolytes, the formation of inactive Li on the Cu surface is due to the loss/interruption of its ionic pathway, rather than electronic. Although operando techniques are invaluable for real-time analysis of the system and enable direct correlation of NMR observations with electrochemical phenomena, the solid and robust nature of materials in solid-state batteries makes ex situ and *postmortem* methods particularly practical and effective for studying the formation and growth of high-surface-area Li within solid electrolytes and their failure mechanism.[125] Importantly, these methods allow the investigation of cells in configurations closer to industrial designs, providing valuable insights that complement *operando* techniques.

Li dissolution, which causes capacity loss in a charged cell even when no current is applied, is a critical phenomenon that can be studied using in situ NMR, monitoring the Li metal intensity with time at open-circuit voltage (OCV). Previous works have explored the impact of electrolyte formulation (Figure 20d), substrate surface, and Li deposit morphology on the Li corrosion rate to highlight the importance of SEI engineering in LIBs, and the advantages of SSBs in preserving the Li metal during aging.[107,106,108,109,111,124,110,101,126] Expanding on that, Gunnarsdóttir et al.[127] conducted ^{6}Li/^{7}Li isotope exchange experiments, tracking the Li exchange between the electrolyte and Li metal in situ to evaluate the transport properties of the SEI, and its correlation with deposit morphology.

Overhauser dynamic nuclear polarization (DNP) is a powerful technique that enhances NMR signal intensity by transferring the high polarization of unpaired electrons to nearby nuclei. Although not inherently quantitative, DNP enables the detection of Li deposits or high-surface-area Li even at low concentrations, which are otherwise challenging to observe.[128] Moreover, it provides valuable insights into the composition and properties of SEI.[128,129] For example, Hope et al.[128] employed DNP to selectively enhance the signals of SEI components in the LP30 electrolyte, both with and without the FEC additive, to investigate the composition and spatial proximity of SEI components to the Li metal surface. More recently, Maity et al.[129] used DNP to study the dendrite propagation paths through various composite polymer electrolytes and indirectly investigated the SEI Li permeability.

While numerous ideas and methods based on NMR spectroscopy have been previously explored, the versatility of this tool continues to offer opportunities for innovations. For instance, the availability of two NMR-active isotopes for lithium (^{6}Li and ^{7}Li) enables many innovations in experiment design by using ^{6}Li-enriched metal foils or Li salts for selective analysis or exchange studies. Furthermore, the discussed NMR and DNP methods could be extended to other battery chemistries such as Na or Mg-based batteries with minimal adaptation.[128] Looking ahead, rapid advancements in spectrometer technology, combined with the ease of Li metal detection via NMR, suggest that benchtop spectrometers might become low-cost and convenient tools for quality control in the battery industry.

3.3. Other Techniques

In addition to titration and NMR, X-ray based techniques[67–71] are valuable tools for studying inactive Li, thanks to their high spatial resolution and operando capabilities. These methods are particularly useful for distinguishing active Li from its inactive forms, helping to identify the mechanisms that lead to capacity loss.

In situ XRD has been used extensively to monitor Li deposition and stripping. For example, Zhu et al.[71] employed XRD to detect residual Li on Cu substrates in AFLMBs, revealing that carbonate-based electrolytes promote more inactive Li formation than ether-based counterparts. Similarly, Geise et al.[69] performed *operando* synchrotron XRD to quantify Li degradation mechanisms (specifically, inactive Li and SEI growth), thereby illustrating key cycling inefficiencies and corrosion processes. Building on these efforts, Shadike et al.[68] combined synchrotron XRD with pair distribution function (PDF) analysis to characterize the SEI. Their work detected crystalline phases such as LiH and LiF, highlighting structural differences between bulk LiF and nanocrystalline SEI-LiF, as well as the influence of electrolyte concentration on inactive Li formation.

A major advancement in X-ray-based characterization came with the development of operando X-ray computed tomography (XCT). Sadd et al.[67] demonstrated the ability of XCT to track the spatial distribution and evolution of Li microstructures in real time. As shown in **Figure 21**a, their approach enabled real-time imaging of Li dynamics within a dedicated Li||Cu electrochemical cell. Notably, certain regions of inactive Li (labeled in green, Figure 21b) were clearly disconnected from the main Li deposit. This operando methodology provided critical insights into how high-surface-area Li growth under various current densities contributes to capacity loss. Although X-ray-based methods deliver indispensable real-time visualization of Li microstructures, they face challenges due to weak X-ray scattering cross-section of Li and the difficulties of analyzing amorphous phases. Ongoing advances in synchrotron facilities and data-processing algorithms are expected to further enhance both resolution and sensitivity.

Fluorescence probing techniques provide another innovative strategy for studying Li metal anodes,[113–115] enabling both

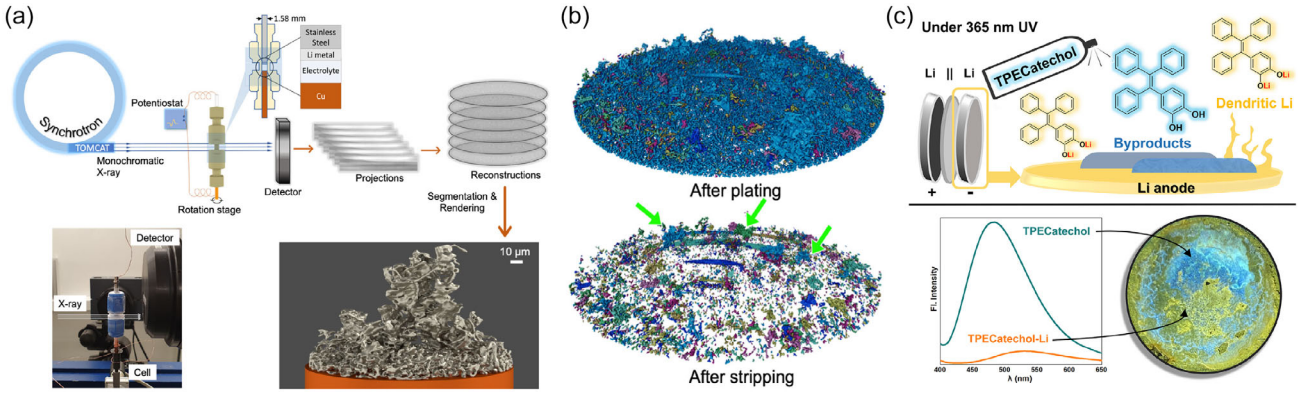

Figure 21. a) Operando XCT setup showing synchrotron-based 3D imaging of Li microstructures during plating and stripping in a Li||Cu electrochemical cell, b) representative reconstructed 3D images of Li microstructures before and after stripping, highlighting regions of inactive Li (green arrows) disconnected from the main Li structure after plating and after stripping at 1.0 mA cm^{-2},[67] and c) fluorescent probing of Li metal using an AIE fluorescence probe (TPECatechol). TPECatechol reacts selectively with active Li, producing a fluorescence shift from cyan to yellow, while retaining its original emission when exposed to SEI or byproducts.[115] Reproduced with permission.[67] Copyright 2023, Springer Nature, and reproduced with permission.[115] Copyright 2022, Elsevier.

visualization and semi-quantification of inactive Li and its byproducts. Fluorochromes or aggregation-induced emission (AIE) probes allow for differentiating between active Li, high-surface-area deposited Li, and inactive Li species.

Cheng et al.[113] introduced 9,10-dimethylanthracene (DMA) as a fluorochrome responsive to Li metal. Fluorescence quenching served as an indicator of active Li distribution, revealing high-surface-area Li formation and byproduct accumulation that can lead to uneven Li deposition and safety risks under high current densities. In line with this concept, Wang et al.[115] developed a solid-state AIE fluorescence probe, TPECatechol, specifically designed to distinguish high-surface-area deposited Li from byproducts. As seen in Figure 21c, the catechol moiety reacts rapidly with Li metal, producing a distinct fluorescence shift that visually highlights high-surface-area Li structures and SEI components. In another advancement, Wang et al.[114] introduced AIE-based fluorescent tracers directly into the electrolyte, facilitating intrinsic fluorescence within the SEI during cycling. This method revealed important details about the SEI distribution, morphology, and evolution, highlighting how it interacts with the Li metal surface and influences overall cell performance.

Despite their promising capabilities, fluorescence techniques are often limited by ex situ or destructive sample preparation, which hinders continuous, operando analysis. Moreover, their ability to probe sub-surface Li remains uncertain, making it challenging to fully characterize the depth and distribution of inactive Li species.

Operando NDP[72,73] is another powerful, nondestructive tool for quantitative characterization of Li microstructures under realistic operating conditions. By exploiting the neutron capture reaction of Li isotopes, NDP offers direct insight into the depth-resolved distribution of Li within battery electrodes. This technique enables real-time monitoring of both inactive and active Li, yielding complementary information to more conventional electrochemical metrics like CE. For example, Lv et al.[73] demonstrated operando NDP to investigate how current density and cycling history influence Li plating and stripping. Contrary to the usual expectation that higher currents produce more porous deposits, their results indicated that under relatively small but increased current densities, Li nucleation becomes denser, forming more compact microstructures. The study also revealed that a fraction of inactive Li can be reactivated during subsequent slower cycling, pointing to a history-dependent interplay between Li deposits and the SEI. NDP has also been used to evaluate how electrolyte additives influence Li deposition, helping to develop strategies for minimizing inactive Li buildup. Despite these advantages, NDP requires specialized facilities and is limited to measuring the total amount of inactive Li, without distinguishing between the inactive Li and the Li within the SEI.

Electrochemical methods are also fundamental for evaluating active Li loss in LMBs, largely due to their simplicity and widespread availability. These approaches deliver macroscopic insights into the sources of irreversible capacity loss, encompassing both inactive Li and SEI formation. Traditional protocols typically involve retrieving cycled electrodes for *postmortem* analysis, measuring the remaining active Li to reflect the cumulative impact of parasitic processes. For example, Li et al.[130] shows that OCV measurements can detect capacity losses resulting from Li corrosion and SEI instability during resting periods. Huang et al.[59] used various cell setups to develop an integrated protocol that systematically deciphers different sources of irreversible CE in AFLMBs. Their work identified the distinct contributions of initial extra SEI formation, inactive Li, subsequent SEI buildup, the cathode's first-cycle intrinsic irreversible capacity, and oxidative electrolyte decomposition. Despite these advances, it is important to note that electrochemical methods generally quantify total inactive Li, combining both inactive Li and Li bound within the SEI.

These complementary methods (X-ray-based 3D imaging, fluorescence probing, and electrochemical measurements) continue to evolve rapidly to clarify the complexities of LMB operation. Further improvements in synchrotron facilities, fluorescence probe design, and data-processing algorithms promise to enhance the resolution, sensitivity, and real-time capabilities of these techniques,

allowing for more detailed characterization of morphological and chemical evolutions. Additionally, integrating these methods with advanced NMR spectroscopy, NDP, or computational modeling could yield a more comprehensive view of inactive Li dynamics. An equally important priority is testing larger cell formats, such as pouch cells or monolayer cells, rather than relying solely on coin cells. Coin cell data can be challenging to translate to commercial LMBs, where differences in cell geometry, electrolyte volumes, and mechanical constraints play critical roles in overall performance and failure mechanisms. By shifting toward more realistic cell designs, the complexities of interface evolution, mechanical stresses, and electrolyte management in industrially relevant systems can better be captured. Overall, the advances in characterization techniques and cell formats will be crucial for developing robust electrolytes, interfaces, and architecture, ultimately pushing LMBs toward longer cycle life, higher energy density, and improved safety. Recent review papers have also offered insightful overviews of various analytical techniques for quantifying inactive Li, and readers are encouraged to refer to these sources for a more detailed discussion.[65,66]

4. Reactivation of Inactive Lithium

Inactive Li, often termed 'dead/isolated Li', has long been recognized as a major contributor to performance decay in LMBs, especially in early-generation electrolytes. Advances in electrolyte formulations have mitigated but not eliminated this challenge. Even with modern electrolytes, inactive Li still forms under conditions of high current densities, low temperatures, low stack pressures, or extended cycling. Understanding and exploiting its potential reactivation, therefore, remains critical to improving battery performance and extending cycle life.

Traditionally, inactive Li has been regarded as definitively inactive, having lost its electrical connectivity with the anode and contributing irreversibly to capacity fading in LMBs.[38] However, recent studies have challenged this long-held assumption, revealing that inactive Li can remain responsive to electric fields within the cell, allowing for dynamic behavior under specific conditions.[131] This finding opens new possibilities for partially recovering the capacity lost due to inactive Li.

Liu et al.[131] provided compelling evidence that the polarization properties of inactive Li enable it to participate dynamically in electrochemical processes, rather than being irrecoverably lost. As demonstrated in **Figure 22**a, their experiments employed an inactive Li island placed between a Li metal anode and a nickel manganese cobalt oxide (NMC) cathode. During the charging process, Li was observed to dissolve from the anode-facing side of the inactive Li island and deposit onto its cathode-facing side, driven by the electric field across the cell (Figure 22b). The process was reversed during discharge, with dissolution occurring on the cathode-facing side and deposition on the anode-facing side. These cyclic deposition-dissolution dynamics caused the inactive Li to "shuttle" between electrodes over time, highlighting its potential for reintegration into the battery's electrochemical processes. Their study also revealed that the efficiency and extent of inactive Li reactivation are influenced by several factors, including the morphology of the inactive Li deposit, the electrolyte composition, and operational parameters such as current density and cycling protocols. As illustrated in Figure 22c, simulations further highlighted the role of electric field gradients in driving these processes. The overpotential across the inactive Li interface plays

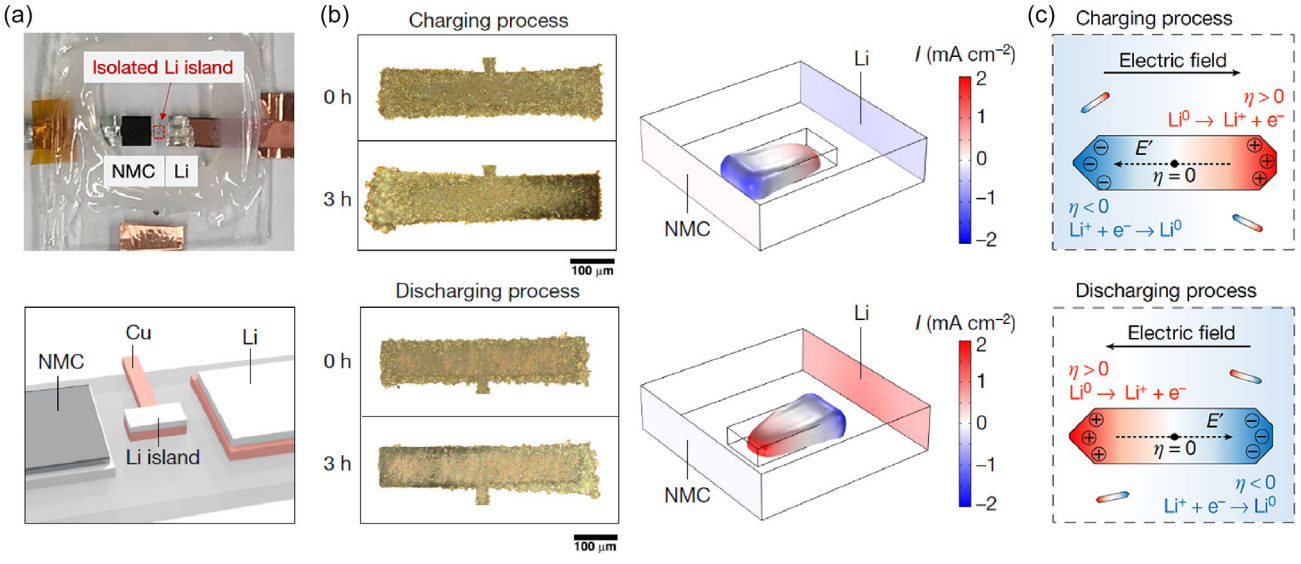

Figure 22. Dynamic behavior and potential recovery of inactive lithium: a) experimental setup and corresponding schematic with an inactive (isolated) Li island positioned between NMC and Li electrodes; b) optical images of the inactive Li island during charging and discharging processes, demonstrating morphological changes at 0 and 3 h; under charging, dissolution occurs on the anode-facing side of inactive Li while deposition takes place on the cathode-facing side, leading to spatial progression towards the cathode, the reverse occurs during discharge; and c) simulation of electric field-induced charge transfer at the inactive Li interface during charging and discharging, illustrating overpotential-driven Li deposition and dissolution.[131] Reproduced with permission.[131] Copyright 2021, Springer Nature.

a crucial role, with positive overpotentials ($\eta > 0$) favoring Li dissolution, while negative overpotentials ($\eta < 0$) facilitate Li deposition. These electric field-induced dynamics provide a mechanistic basis for observed behavior and underscore the possibility of designing strategies to recover a portion of inactive Li during cycling. This study not only provides a deeper understanding of the behavior of inactive Li but also challenges the traditional perception of "dead/isolated Li" as a permanent loss.

4.1. Electrochemical Protocols for Reactivation

Different electrochemical protocols have been investigated to encourage the reactivation of inactive Li. By tailoring cycling designs, the interplay between operating conditions and the dynamic behavior of inactive Li could be optimized.

4.1.1. Short, High-Current Discharges

Building upon the polarization-driven mobility of inactive Li, Liu et al.[131] introduced an innovative protocol involving short, high-current stripping steps at the beginning of discharge cycles (**Figure 23**a). This method promotes the reconnection of previously inactive Li to the active electrode, effectively reincorporating it into the electrochemical cycle. Cells employing this protocol demonstrated prolonged cycle life, achieving stable cycling for over 40 cycles compared to 30 cycles without activation. The 29% increase in cycle life highlights the potential of targeted high-current pulses to partially recover inactive Li and extend the cycle life.

4.1.2. Resting in the Discharged State

Another promising strategy for reviving inactive Li is to include resting periods when the cell is in a discharged state. Zhang et al.[132] demonstrated that this approach partially dissolves SEI components, reducing interfacial impedance and exposing additional surfaces of inactive Li to active sites (Figure 23b). Operando optical microscopy revealed morphological changes in both the inactive Li deposits and the surrounding SEI during these rest intervals. As the organic SEI layers gradually broke down, previously inactive Li re-established its contact with the current collector, leading to enhanced capacity retention and CE.

4.1.3. Self-Heating at High Current Densities

In a complementary approach, Li et al.[133] observed that operating at current densities above 9 mA cm^{-2} induces localized Joule heating, which increases Li surface diffusion. This mechanism facilitates the fusion of dendritic structures into smoother morphologies, effectively "reconditioning" inactive Li into active material. Evaluations in Li||Li symmetric cells and Li-sulfur batteries confirmed that this strategy improves CE and capacity recovery (Figure 23c).

Despite promising laboratory results,[134] the real-world implementation of these reactivation strategies remains challenging. Discharge behavior in consumer applications, for example, is largely user-dependent, making it difficult to standardize protocols such as resting in a discharged state. Nevertheless, adaptive battery management systems (BMS) might potentially integrate periodic rest intervals or controlled discharge profiles to help recover inactive Li. In industrial or grid-scale settings, where usage patterns are more controlled, these protocols may be more easily adopted. Future studies will likely involve refining electrolyte formulations, optimizing cycling parameters, and developing intelligent BMS algorithms to systematically harness the dynamic behavior of inactive Li for improved battery performance.

4.2. Redox Mediators for Reviving Inactive Li

In addition to electrochemical protocols, redox mediators also offer a compelling approach to recover inactive Li.[135–137] By using carefully chosen redox-active species, these mediators can

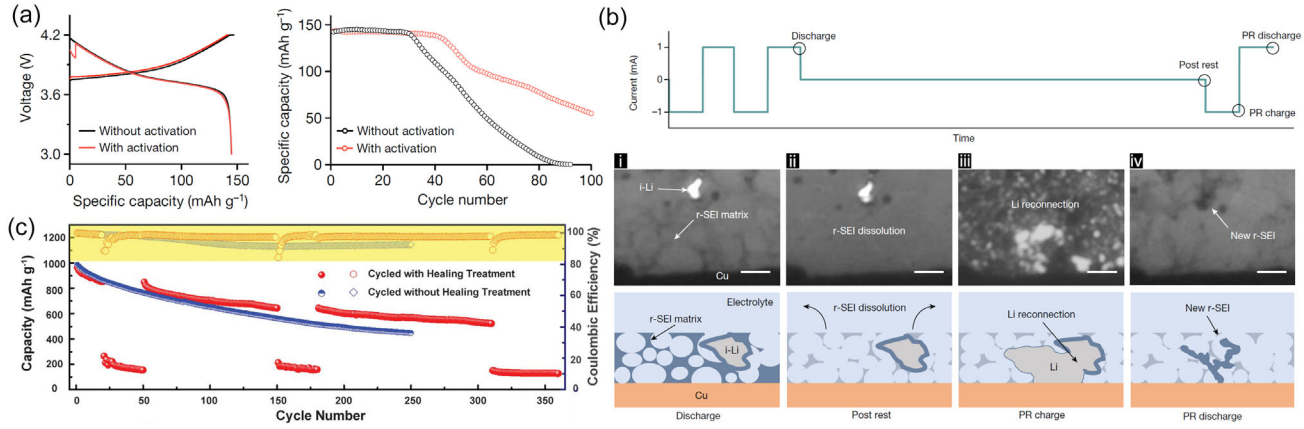

Figure 23. Electrochemical strategies for reactivating of inactive lithium: a) voltage-capacity profiles and cycling stability comparison of cells with and without activation protocols, demonstrating improved extended cycle life with activation;[131] b) operando optical images and schematic illustrate the reactivation process of inactive Li (isolated Li, i-Li): i) r-SEI matrix formation, ii) r-SEI dissolution during rest, iii) Li reconnection, and iv) new r-SEI formation after the post-rest (PR) discharge (scale bars: 5 μm).[132] c) Long-term cycling results comparing cells with and without healing treatments, showing enhanced capacity retention and CE for treated cells.[133] Reproduced with permission.[131] Copyright 2021 and reproduced with permission.[132] Copyright 2024, Springer Nature, and reproduced with permission.[133] Copyright 2018, American Association for the Advancement of Science.

dissolve or oxidize inactive Li, converting it into ionic forms that reintegrate into the electrochemical cycle.

Jin et al.[135] demonstrated how iodine-based redox chemistry can restore inactive Li via triiodide ions (I_3^-). As shown in **Figure 24**, these ions spontaneously react with inactive Li sources, such as Li_2O and Li metal debris within the SEI, forming soluble Li iodide (LiI) and iodate species ($LiIO_3$). The formed $LiIO_3$ works as an oxygen shuttle, facilitating the regeneration of a stable SEI on the anode. Upon reduction by active Li metal, in fact, $LiIO_3$ converts to Li_2O and LiI. Li_2O strengthens the SEI, while soluble LiI migrates to the cathode to regenerate I_3^-, thus completing a self-sustaining redox cycle that both recycles inactive Li and stabilizes the SEI.

Reactivating inactive Li is even more critical in AFLMBs than in conventional LMBs. The absence of a Li reservoir in AFLMBs means that any Li sequestered as electronically isolated Li^0 or Li_2O represents a permanent loss of cyclable Li, rapidly accelerating capacity fade. To address this, Dong et al. implemented an iodine-based redox mediator strategy by embedding strontium iodide (SrI_2) in the current collector.[138] This design enabled continuous reactivation of inactive Li via the I^-/I_3^- redox couple, while simultaneously forming a LiI/SrF_2-rich SEI that mitigated further electrolyte degradation. As a result, NCM532 AFLMB pouch cells demonstrated stable cycling over 200 cycles with a remarkably low-capacity fade rate of just 0.09% per cycle. These findings highlight that iodine-based redox mediation is not only compatible with anode-free architectures but may be essential for their long-term stability, where recovery of every Li ion is crucial for maintaining performance and enabling practical deployment.

In parallel, Zhang et al.[136] introduced 2,2,6,6-tetramethylpiperidine-1-oxyl (TEMPO) as an effective redox mediator. During charging, TEMPO oxidizes to $TEMPO^+$ cations, which diffuse through the electrolyte and oxidize inactive Li, converting it into Li^+ ions. Similarly, a study by Huang et al. examined redox mediators such as ferrocene (Fc), 10-methylphenothiazine (MPT), and thianthrene (Th), demonstrating the importance of selecting a mediator with an optimal redox potential.

Overall, redox mediators typically proceed via two main steps. In step (I), the oxidized mediator species reacts with inactive Li, oxidizing it to Li^+ ions and becoming reduced in the process. In step (II), the reduced mediator migrates to the cathode during charging, where it donates electrons (or is re-oxidized), thus regenerating its active form and closing the redox loop. For

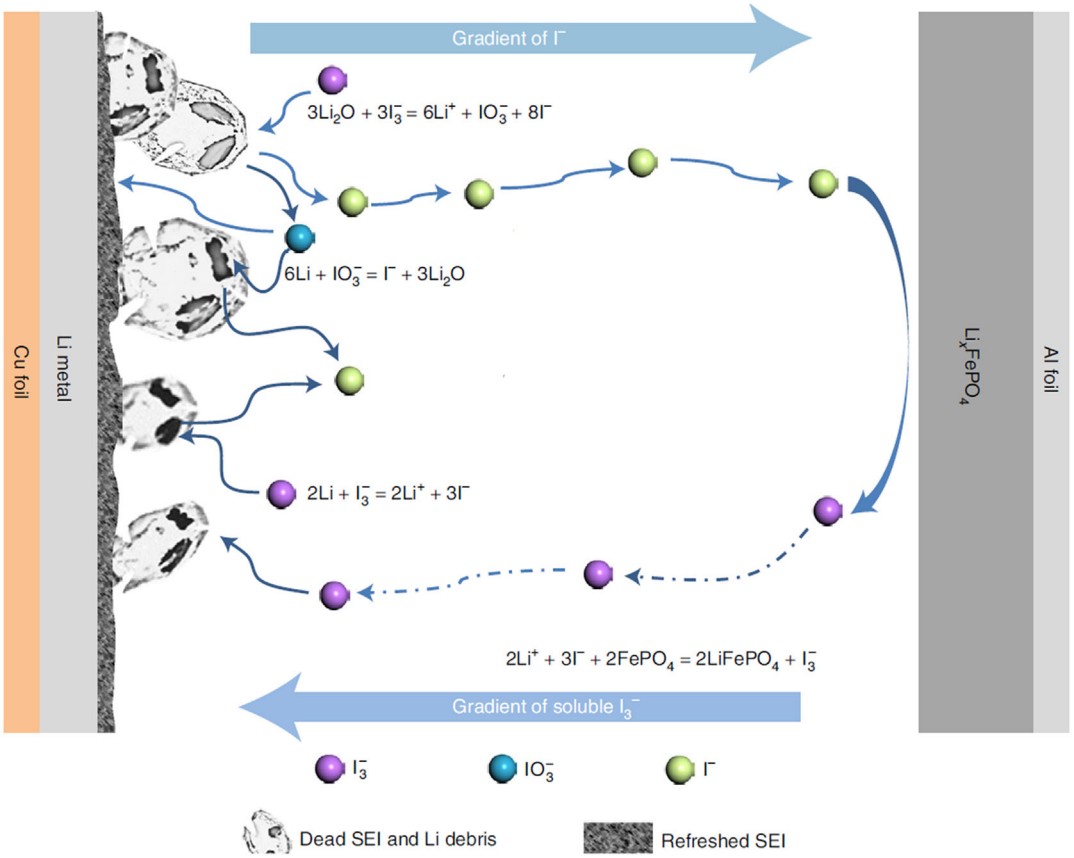

Figure 24. Lithium reactivation via iodine redox shuttling: inactive li in the "dead" SEI is removed by the I_3^- additive, forming soluble lil and IO_3^-. $LiIO_3$ is then reduced by Li metal to produce Li_2O and LiI. The newly formed Li_2O deposits onto the anode, contributing to a refreshed SEI. An "oxygen shuttle" mechanism transfers oxygen from the Li_2O in the dead SEI back to the anode, rejuvenating the SEI. Additionally, I_3^- reacts with Li debris to produce LiI. All released Li is transported to the cathode as LiI and returned to the anode during charging. At the cathode, LiI reacts with delithiated $LiFePO_4$ (LFP) to regenerate I_3^-, which diffuses back to the anode to sustain the SEI restoration and Li reactivation process.[135] Reproduced with permission.[135] Copyright 2021, Springer Nature.

sustained cycling, the redox potential of the mediator must be 1) lower than the charge cut-off voltage, ensuring that the mediator can be re-oxidized repeatedly without premature decomposition, and 2) higher than the cathode's redox potential, preventing self-discharge and minimizing energy loss. By tuning these parameters, researchers can leverage redox mediators to effectively recover inactive Li, potentially improving capacity retention and extending battery cycle life without substantially compromising the overall performance.

5. Conclusions and Perspectives

This review highlights the multifaceted challenges and emerging strategies for the formation and reactivation of inactive Li in LMBs, as schematically illustrated in Figure 1 Figure 1. Inactive Li emerges from intricate interfacial processes, including SEI degradation, high-surface-area Li growth, and eventual electrochemical isolation. These phenomena are driven by key operating parameters such as current density, pressure, electrolyte composition, and temperature, which collectively contribute to capacity fade, cycling instability, and safety concerns. Understanding the interplay between SEI chemistry, Li morphology, and electrolyte dynamics remains a critical research gap. Advanced computational models, integrated with experimental data, could provide deeper insights into these mechanisms, enabling the development of more targeted mitigation strategies.

Despite significant progress in avoiding the formation of high-surface-area lithium, challenges persist in pouch cell level under harsh conditions such as low temperatures, low stack pressures, and low amount of electrolyte, where inactive Li formation becomes unavoidable. In such scenarios, strategies for reactivating inactive Li gain importance, providing a means to recover capacity and maintain battery performance in demanding environments. In these scenarios, inactive Li must be effectively managed to sustain capacity and ensure long-term battery performance. Reactivation strategies, while not a replacement for prevention, become essential tools for mitigating capacity loss when prevention alone is insufficient. Simultaneously, adapting advanced diagnostic setups for commercial cell formats, such as pouch cells, is critical. These setups must account for the unique thermal and mechanical conditions of larger batteries while enabling real-time monitoring. By combining preventative and reactive strategies with scalable diagnostics, the gap between laboratory-scale research and industrial application can be effectively bridged, fostering the practical implementation of high-performance LMBs technologies.

Accurate quantification of inactive Li remains a fundamental challenge, as it is critical for understanding its dynamics and impact on battery performance. Techniques such as solid-state NMR, titration gas chromatography, ICP-OES, and advanced imaging methods such as *operando* synchrotron XRD have shown promise in providing detailed insights into inactive Li evolution. In parallel, emerging reactivation strategies are coalescing around two complementary pathways: 1) electrochemical conditioning protocols and 2) redox-mediated chemical loops. Electrochemical protocols apply targeted current or voltage profiles, such as self-heating pulses, high-current stripping bursts, or controlled rest periods at specific state-of-charge windows, to leverage the residual polarizability of electrically isolated Li and gradually reincorporate it into the active inventory. Redox-mediated approaches, on the other hand, employ soluble shuttle mediators that can chemically oxidize disconnected Li^0 or Li_2O and re-lithiate the cathode in a closed-loop mechanism. Successful implementation of these strategies requires careful matching of the mediator's redox potential to the voltage window of the cell, along with chemical compatibility with both the electrolyte and SEI.

Coupled with ongoing advances in electrolyte formulation, interface engineering, and separator design, such reactivation strategies offer a promising route to sustain coulombic efficiency and delay capacity fade. The same principles are pertinent to other high-energy chemistries, including lithium–sulfur and solid-state systems, where the accumulation of inactive material likewise constrains lifetime. Continued integration of high-resolution diagnostics with scalable mitigation and reactivation protocols will therefore be critical to translating laboratory insights into durable, high-performance energy-storage technologies.

Acknowledgements

The Alistore-European Research Institute (ALISTORE-ERI) network is warmly thanked. The authors gratefully acknowledge financial support from the French National Research Agency (project Labex STORE-EX, ANR-10-LABX-76-01). P.G. as a part of the DESTINY Ph.D. program acknowledges funding from the European Union's Horizon 2020 research and innovation program under the Marie Skłodowska–Curie Actions COFUND–grant agreement no: 945357.

Conflict of Interest

The authors declare no conflict of interest.

Keywords: coulombic efficiency · dendrite growth · inactive lithium formation · lithium metal batteries · lithium quantification techniques · reactivation strategies · solid electrolyte interphase

[1] X.-B. Cheng, R. Zhang, C.-Z. Zhao, Q. Zhang, *Chem. Rev.* **2017**, *117*, 10403.
[2] P. Zou, Y. Sui, H. Zhan, C. Wang, H. L. Xin, H.-M. Cheng, F. Kang, C. Yang, *Chem. Rev.* **2021**, *121*, 5986.
[3] Y. Xu, K. Dong, Y. Jie, P. Adelhelm, Y. Chen, L. Xu, P. Yu, J. Kim, Z. Kochovski, Z. Yu, W. Li, J. LeBeau, Y. Shao-Horn, R. Cao, S. Jiao, T. Cheng, I. Manke, Y. Lu, *Adv. Energy Mater.* **2022**, *12*, 2200398.
[4] B. Horstmann, J. Shi, R. Amine, M. Werres, X. He, H. Jia, F. Hausen, I. Cekic-Laskovic, S. Wiemers-Meyer, J. Lopez, D. Galvez-Aranda, F. Baakes, D. Bresser, C.-C. Su, Y. Xu, W. Xu, P. Jakes, R.-A. Eichel, E. Figgemeier, U. Krewer, J. M. Seminario, P. B. Balbuena, C. Wang, S. Passerini, Y. Shao-Horn, M. Winter, K. Amine, R. Kostecki, A. Latz, *Energy Environ. Sci.* **2021**, *14*, 5289.
[5] W. Xu, J. Wang, F. Ding, X. Chen, E. Nasybulin, Y. Zhang, J.-G. Zhang, *Energy Environ. Sci.* **2014**, *7*, 513.
[6] J. Li, Z. Kong, X. Liu, B. Zheng, Q. H. Fan, E. Garratt, T. Schuelke, K. Wang, H. Xu, H. Jin, *InfoMat* **2021**, *3*, 1333.

[7] Y. Chen, Y. Luo, H. Zhang, C. Qu, H. Zhang, X. Li, *Small Methods* **2019**, *3*, 1800551.
[8] C. Monroe, J. Newman, *J. Electrochem. Soc.* **2003**, *150*, A1377.
[9] J.-N. Chazalviel, *Phys. Rev. A* **1990**, *42*, 7355.
[10] J. Yamaki, S. Tobishima, K. Hayashi, S. Keiichi, Y. Nemoto, M. Arakawa, *J. Power Sources* **1998**, *74*, 219.
[11] S. E. Sandoval, C. G. Haslam, B. S. Vishnugopi, D. W. Liao, J. S. Yoon, S. H. Park, Y. Wang, D. Mitlin, K. B. Hatzell, D. J. Siegel, P. P. Mukherjee, N. P. Dasgupta, J. Sakamoto, M. T. McDowell, *Nat. Mater.* **2025**, *24*, 674.
[12] P. Zhai, L. Liu, X. Gu, T. Wang, Y. Gong, *Adv. Energy Mater.* **2020**, *10*, 2001257.
[13] A. Pei, G. Zheng, F. Shi, Y. Li, Y. Cui, *Nano Lett.* **2017**, *17*, 1132.
[14] A. J. Sanchez, E. Kazyak, Y. Chen, K.-H. Chen, E. R. Pattison, N. P. Dasgupta, *ACS Energy Lett.* **2020**, *5*, 994.
[15] L. Lin, H. Zheng, Q. Luo, J. Lin, L. Wang, Q. Xie, D.-L. Peng, J. Lu, *Adv. Funct. Mater.* **2024**, *34*, 2315201.
[16] S. Jo, B. Kwon, J. Oh, J. Lee, K. Park, K. T. Lee, *J. Mater. Chem. A* **2022**, *10*, 5520.
[17] P. Biswal, S. Stalin, A. Kludze, S. Choudhury, L. A. Archer, *Nano Lett.* **2019**, *19*, 8191.
[18] J. Zhang, A. F. Chadwick, P. W. Voorhees, *Cell Rep. Phys. Sci.* **2025**, *6*, 102360.
[19] D. R. Ely, A. Jana, R. E. García, *J. Power Sources* **2014**, *272*, 581.
[20] K. Cai, M. Zhang, G. Zhong, G. Kang, J. Biao, C. Li, Y. Liu, G. Zhou, F. Kang, Y. Cao, *J. Mater. Chem. A* **2024**, *12*, 11719.
[21] A. Mohammadi, L. Monconduit, L. Stievano, R. Younesi, *J. Electrochem. Soc.* **2022**, *169*, 070509.
[22] A. Mohammadi, S. Djafer, S. Sayegh, A. J. Naylor, M. Bechelany, R. Younesi, L. Monconduit, L. Stievano, *Chem. Mater.* **2023**, *35*, 2381.
[23] J. Rizell, W. Chrobak, N. Mozhzhukhina, S. Xiong, A. Matic, *J. Electrochem. Soc.* **2024**, *171*, 020517.
[24] J. Seok, C. N. Gannett, S.-H. Yu, H. D. Abruña, *Anal. Chem.* **2021**, *93*, 15459.
[25] J.-H. Hyun, M.-J. Yi, H. Jung, S.-H. Lee, J. H. Um, S.-H. Yu, *Energy Storage Mater.* **2023**, *54*, 146.
[26] A. J. Sanchez, E. Kazyak, Y. Chen, K. H. Chen, E. R. Pattison, N. P. Dasgupta, *Morphology, and Reversibility. ACS Energy Lett.* **2020**, *5*, 994.
[27] Y. Gu, H. Yan, W.-W. Wang, X.-G. Zhang, J. Yan, B.-W. Mao, *Nano Lett.* **2023**, *23*, 9872.
[28] K. Yan, J. Wang, S. Zhao, D. Zhou, B. Sun, Y. Cui, G. Wang, *Angew. Chem., Int. Ed.* **2019**, *58*, 11364.
[29] J. Wang, W. Huang, A. Pei, Y. Li, F. Shi, X. Yu, Y. Cui, *Nat. Energy* **2019**, *4*, 664.
[30] D. R. Ely, R. E. García, *J. Electrochem. Soc.* **2013**, *160*, A662.
[31] X. Sun, X. Zhang, Q. Ma, X. Guan, W. Wang, J. Luo, *Angew. Chem., Int. Ed.* **2020**, *59*, 6665.
[32] K. Yan, Z. Lu, H.-W. Lee, F. Xiong, P.-C. Hsu, Y. Li, J. Zhao, S. Chu, Y. Cui, *Nat. Energy* **2016**, *1*, 16010.
[33] A. Mohammadi, A. Hagopian, S. Sayegh, M. Bechelany, J.-S. Filhol, R. Younesi, L. Stievano, L. Monconduit, *J. Mater. Chem. A* **2022**, *10*, 17593.
[34] K. N. Wood, E. Kazyak, A. F. Chadwick, K.-H. Chen, J.-G. Zhang, K. Thornton, N. P. Dasgupta, *ACS Cent. Sci.* **2016**, *2*, 790.
[35] P. Bai, J. Li, F. R. Brushett, M. Z. Bazant, *Energy Environ. Sci.* **2016**, *9*, 3221.
[36] L. Frenck, G. K. Sethi, J. A. Maslyn, N. P. Balsara, *Front. Energy Res.* **2019**, *7*, 115.
[37] J. Steiger, D. Kramer, R. Mönig, *J. Power Sources* **2014**, *261*, 112.
[38] Q. Li, H. Liu, F. Wu, L. Li, Y. Ye, R. Chen, *Angew. Chem., Int. Ed.* **2024**, *63*, e202404554.
[39] Y. Liu, X. Xu, M. Sadd, O. O. Kapitanova, V. A. Krivchenko, J. Ban, J. Wang, X. Jiao, Z. Song, J. Song, S. Xiong, A. Matic, *Adv. Sci.* **2021**, *8*, 2003301.
[40] D. T. Boyle, Y. Li, A. Pei, R. A. Vilá, Z. Zhang, P. Sayavong, M. S. Kim, W. Huang, H. Wang, Y. Liu, R. Xu, R. Sinclair, J. Qin, Z. Bao, Y. Cui, *Nano Lett.* **2022**, *22*, 8224.
[41] Y. Zhang, W. Bao, E. Jeffs, B. Liu, B. Han, W. Mai, X. Li, W. Li, Y. Xu, B. Bhamwala, A. Liu, L. Ah, K. Ryu, Y. S. Meng, H. Gan, *ACS Energy Lett.* **2025**, *10*, 872.
[42] A. Kushima, K. P. So, C. Su, P. Bai, N. Kuriyama, T. Maebashi, Y. Fujiwara, M. Z. Bazant, J. Li, *Nano Energy* **2017**, *32*, 271.
[43] W. S. LePage, Y. Chen, E. Kazyak, K.-H. Chen, A. J. Sanchez, A. Poli, E. M. Arruda, M. D. Thouless, N. P. Dasgupta, *J. Electrochem. Soc.* **2019**, *166*, A89.
[44] M. A. Thorpe, M. Zhang, D. W. Liao, S. E. Sandoval, Y. Kim, M. T. McDowell, M. D. Thouless, N. P. Dasgupta, *Matter* **2025**, *8*, 101955.
[45] Y. He, X. Ren, Y. Xu, M. H. Engelhard, X. Li, J. Xiao, J. Liu, J.-G. Zhang, W. Xu, C. Wang, *Nat. Nanotechnol.* **2019**, *14*, 1042.
[46] K. Jiang, K.-H. Kim, B. Gallant, *Joule* **2024**, *9*, 101963.
[47] V. Müller, R.-G. Scurtu, M. Memm, M. A. Danzer, M. Wohlfahrt-Mehrens, *J. Power Sources* **2019**, *440*, 227148.
[48] C. Soulen, N. Lam, J. Holoubek, P. Liu, *J. Electrochem. Soc.* **2024**, *171*, 020535.
[49] D. Liu, B. Wu, Y. Xu, J. Ellis, A. Baranovskiy, D. Lu, J. Lochala, C. Anderson, K. Baar, D. Qu, J. Yang, D. Galvez-Aranda, K.-J. Lopez, P. B. Balbuena, J. M. Seminario, J. Liu, J. Xiao, *Nat. Energy* **2024**, *9*, 559.
[50] C. M. Efaw, Z. Wang, H. Zhang, P. L. Barnes, L. Xu, Y. Wang, D. Olds, S. Kim, B. Park, A. Narla, H. Xiong, E. J. Dufek, P. G. Khalifah, H. Xu, B. Li, *Device* **2025**, *3*, 100660.
[51] X. Gao, Y.-N. Zhou, D. Han, J. Zhou, D. Zhou, W. Tang, J. B. Goodenough, *Joule* **2020**, *4*, 1864.
[52] H. H. Yan, Y. H. Bie, X. Y. Cui, G. P. Xiong, L. Chen, *Energy Convers. Manage.* **2018**, *161*, 193.
[53] Y. Li, W. Huang, Y. Li, A. Pei, D. T. Boyle, Y. Cui, *Joule* **2018**, *2*, 2167.
[54] M. Werres, Y. Xu, H. Jia, C. Wang, W. Xu, A. Latz, B. Horstmann, *ACS Nano* **2023**, *17*, 10218.
[55] A. Dutta, E. Mizuki, Y. Tomori, S. Matsuda, *ACS Appl. Energy Mater.* **2024**, *7*, 3824.
[56] C. Fang, J. Li, M. Zhang, Y. Zhang, F. Yang, J. Z. Lee, M. H. Lee, J. Alvarado, M. A. Schroeder, Y. Yang, B. Lu, N. Williams, M. Ceja, L. Yang, M. Cai, J. Gu, K. Xu, X. Wang, Y. S. Meng, *Nature* **2019**, *572*, 511.
[57] H. Liu, X.-B. Cheng, R. Xu, X.-Q. Zhang, C. Yan, J.-Q. Huang, Q. Zhang, *Adv. Energy Mater.* **2019**, *9*, 1902254.
[58] K. H. Chen, K. N. Wood, E. Kazyak, W. S. Lepage, A. L. Davis, A. J. Sanchez, N. P. Dasgupta, *J. Mater. Chem. A* **2017**, *5*, 11671.
[59] C. J. Huang, B. Thirumalraj, H. C. Tao, K. N. Shitaw, H. Sutiono, T. T. Hagos, T. T. Beyene, L. M. Kuo, C. C. Wang, S. H. Wu, W. N. Su, B. J. Hwang, *Nat. Commun.* **2021**, *12*.
[60] H. Zhang, M. Ulusel, F. Shi, *ACS Appl. Mater. Interfaces* **2024**, *16*, 66971.
[61] Y. Lu, C.-Z. Zhao, J.-K. Hu, S. Sun, H. Yuan, Z.-H. Fu, X. Chen, J.-Q. Huang, M. Ouyang, Q. Zhang, *Sci. Adv.* **2025**, *8*, eadd0510.
[62] Y.-K. Huang, R. Pan, D. Rehnlund, Z. Wang, L. Nyholm, *Adv. Energy Mater.* **2021**, *11*, 2003674.
[63] X. Cao, X. Ren, L. Zou, M. H. Engelhard, W. Huang, H. Wang, B. E. Matthews, H. Lee, C. Niu, B. W. Arey, Y. Cui, C. Wang, J. Xiao, J. Liu, W. Xu, J.-G. Zhang, *Nat. Energy* **2019**, *4*, 796.
[64] C.-X. Bi, Y.-J. Zhu, Z. Li, M. Zhao, X.-Q. Zhang, B.-Q. Li, J.-Q. Huang, *Adv. Energy Mater.* **2024**, *14*, 2402609.
[65] Z. Zheng, X. Fang, W. Deng, P. Li, X. Zheng, H. Zhang, L. Li, S. Chou, Y. Chen, Y. Tang, J. Wang, *Energy Environ. Sci.* **2024**, *17*, 9051.
[66] M. Tao, J. Chen, H. Lin, Y. Zhou, D. Zhao, P. Shan, Y. Jin, Y. Yang, *J. Energy Chem.* **2024**, *96*, 226.
[67] M. Sadd, S. Xiong, J. R. Bowen, F. Marone, A. Matic, *Nat. Commun.* **2023**, *14*, 854.
[68] Z. Shadike, H. Lee, O. Borodin, X. Cao, X. Fan, X. Wang, R. Lin, S.-M. Bak, S. Ghose, K. Xu, C. Wang, J. Liu, J. Xiao, X.-Q. Yang, E. Hu, *Nat. Nanotechnol.* **2021**, *16*, 549.
[69] N. R. Geise, R. M. Kasse, J. Nelson Weker, H.-G. Steinrück, M. F. Toney, *Chem. Mater.* **2021**, *33*, 7537.
[70] A. Klein, M. Sadd, N. Mozhzhukhina, M. Olsson, L. Broche, S. Xiong, A. Matic, *Batter Supercaps* **2024**, *7*, e202400070.
[71] W. Zhu, H. Demers, G. Girard, D. Clement, F. Zimin, A. Guerfi, M. Trudeau, A. Vijh, A. Paolella, *J. Power Sources* **2022**, *546*, 231941.
[72] G. Zheng, Y. Xiang, S. Chen, S. Ganapathy, T. W. Verhallen, M. Liu, G. Zhong, J. Zhu, X. Han, W. Wang, W. Zhao, M. Wagemaker, Y. Yang, *Energy Storage Mater.* **2020**, *29*, 377.
[73] S. Lv, T. Verhallen, A. Vasileiadis, F. Ooms, Y. Xu, Z. Li, Z. Li, M. Wagemaker, *Nat. Commun.* **2018**, *9*, 2152.
[74] C. Fang, J. Li, M. Zhang, Y. Zhang, F. Yang, J. Z. Lee, M.-H. Lee, J. Alvarado, M. A. Schroeder, Y. Yang, B. Lu, N. Williams, M. Ceja, L. Yang, M. Cai, J. Gu, K. Xu, X. Wang, Y. S. Meng, *Nature* **2019**, *572*, 511.
[75] X.-R. Chen, C. Yan, J.-F. Ding, H.-J. Peng, Q. Zhang, *J. Energy Chem.* **2021**, *62*, 289.
[76] B. Sreenarayanan, D. H. S. Tan, S. Bai, W. Li, W. Bao, Y. S. Meng, *J. Power Sources* **2022**, *531*, 231327.
[77] Z. Yang, W. Liu, Q. Chen, X. Wang, W. Zhang, Q. Zhang, J. Zuo, Y. Yao, X. Gu, K. Si, K. Liu, J. Wang, Y. Gong, *Adv. Mater.* **2023**, *35*, 2210130.
[78] B. Lu, W. Li, D. Cheng, B. Bhamwala, M. Ceja, W. Bao, C. Fang, Y. S. Meng, *Adv. Energy Mater.* **2022**, *12*, 2202012.
[79] R. Xu, J.-F. Ding, X.-X. Ma, C. Yan, Y.-X. Yao, J.-Q. Huang, *Adv. Mater.* **2021**, *33*, 2105962.

[80] S. Zhang, J.-F. Ding, R. Xu, Y. Xiao, C. Yan, J.-Q. Huang, *Adv. Energy Mater.* **2024**, *14*, 2303726.
[81] Z. Zhu, X. Li, X. Qi, J. Ji, Y. Ji, R. Jiang, C. Liang, D. Yang, Z. Yang, L. Qie, Y. Huang, *Nanomicro Lett.* **2023**, *15*, 234.
[82] E. Adhitama, A. D. Refino, T. Brake, J. Pleie, C. Schmidt, F. Demelash, K. Neuhaus, S. Bornemann, S. Wiemers-Meyer, E. Peiner, M. Winter, H. S. Wasisto, T. Placke, *J. Mater. Chem. A* **2023**, *11*, 7724.
[83] C. Gong, S. D. Pu, S. Zhang, Y. Yuan, Z. Ning, S. Yang, X. Gao, C. Chau, Z. Li, J. Liu, L. Pi, B. Liu, I. Capone, B. Hu, D. L. R. Melvin, M. Pasta, P. G. Bruce, A. W. Robertson, *Energy Environ. Sci.* **2023**, *16*, 535.
[84] Y. Xie, Y. Huang, Y. Zhang, T. Wu, S. Liu, M. Sun, B. Lee, Z. Lin, H. Chen, P. Dai, Z. Huang, J. Yang, C. Shi, D. Wu, L. Huang, Y. Hua, C. Wang, S. Sun, *Nat. Commun.* **2023**, *14*, 2883.
[85] Y. Xiang, M. Tao, X. Chen, P. Shan, D. Zhao, J. Wu, M. Lin, X. Liu, H. He, W. Zhao, Y. Hu, J. Chen, Y. Wang, Y. Yang, *Nat. Commun.* **2023**, *14*, 177.
[86] U. Pal, D. Rakov, B. Lu, B. Sayahpour, F. Chen, B. Roy, D. R. MacFarlane, M. Armand, P. C. Howlett, Y. S. Meng, M. Forsyth, *Energy Environ. Sci.* **2022**, *15*, 1907.
[87] J.-F. Ding, R. Xu, X.-X. Ma, Y. Xiao, Y.-X. Yao, C. Yan, J.-Q. Huang, *Angew. Chem., Int. Ed.* **2022**, *61*, e202115602.
[88] H. Chen, Y. Zhao, X. Zhang, R. Li, A. Wang, H. Zhang, J. Liu, B. Wen, L. Zhang, Q. Hua, T. Liu, K. Wu, K. Amine, J. Luo, *Nat. Synth.* **2025**, *4*, 552.
[89] C. Gervillié-Mouravieff, L. Ah, A. Liu, C.-J. Huang, Y. S. Meng, *ACS Energy Lett.* **2024**, *9*, 1693.
[90] M. Tao, Y. Xiang, D. Zhao, P. Shan, Y. Yang, *Commun. Mater.* **2022**, *3*, 50.
[91] W. Deng, X. Yin, W. Bao, X. Zhou, Z. Hu, B. He, B. Qiu, Y. S. Meng, Z. Liu, *Nat. Energy* **2022**, *7*, 1031.
[92] G. M. Hobold, C. Wang, K. Steinberg, Y. Li, B. M. Gallant, *Nat. Energy* **2024**, *9*, 580.
[93] G. M. Hobold, B. M. Gallant, *ACS Energy Lett.* **2022**, *7*, 3458.
[94] M. A. Weret, S.-K. Jiang, K. N. Shitaw, C.-Y. Chang, T. M. Tekaligne, J.-C. Chiou, S.-C. Yang, N. T. Temesgen, Y. Nikodimos, S.-H. Wu, C.-C. Wang, W.-N. Su, B. J. Hwang, *ACS Energy Lett.* **2023**, *8*, 2817.
[95] C. Gong, S. D. Pu, X. Gao, S. Yang, J. Liu, Z. Ning, G. J. Rees, I. Capone, L. Pi, B. Liu, G. O. Hartley, J. Fawdon, J. Luo, M. Pasta, C. R. M. Grovenor, P. G. Bruce, A. W. Robertson, *Adv. Energy Mater.* **2021**, *11*, 2003118.
[96] Y. Zhao, Y. Wu, H. Liu, S.-L. Chen, S.-H. Bo, *ACS Appl. Mater. Interfaces* **2021**, *13*, 35750.
[97] B. Lu, E. Olivera, J. Scharf, M. Chouchane, C. Fang, M. Ceja, L. E. Pangilinan, S. Zheng, A. Dawson, D. Cheng, W. Bao, O. Arcelus, A. A. Franco, X. Li, S. H. Tolbert, Y. S. Meng, *ACS Appl. Energy Mater.* **2021**, *4*, 6454.
[98] M. Tao, Y. Xiang, D. Zhao, P. Shan, Y. Sun, Y. Yang, *Nano Lett.* **2022**, *22*, 6775.
[99] L. Liu, Y. Xiang, J. Wang, *Cell to Atomic Level: Understanding the Degradation in 99% Coulombic Efficiency and 450 Wh Kg^{-1} Anode-Free Pouch Cells* **2024**, https://doi.org/10.26434/chemrxiv-2024-pzdws.
[100] G. Xu, J. Li, C. Wang, X. Du, D. Lu, B. Xie, X. Wang, C. Lu, H. Liu, S. Dong, G. Cui, L. Chen, *Angew. Chem., Int. Ed.* **2021**, *60*, 7770.
[101] Y. Xiang, M. Tao, G. Zhong, Z. Liang, G. Zheng, X. Huang, X. Liu, Y. Jin, N. Xu, M. Armand, J.-G. Zhang, K. Xu, R. Fu, Y. Yang, *Sci. Adv.* **2025**, *7*, eabj3423.
[102] R. Xu, S. Zhang, X. Shen, N. Yao, J.-F. Ding, Y. Xiao, L. Xu, C. Yan, J.-Q. Huang, *Small Struct.* **2023**, *4*, 2200400.
[103] M.-Y. Zhou, X.-Q. Ding, J.-F. Ding, L.-P. Hou, P. Shi, J. Xie, B.-Q. Li, J.-Q. Huang, X.-Q. Zhang, Q. Zhang, *Joule* **2022**, *6*, 2122.
[104] Y.-C. Hsieh, M. Leißing, S. Nowak, B.-J. Hwang, M. Winter, G. Brunklaus, *Cell Rep. Phys. Sci.* **2020**, *1*, 100139.
[105] B. Zheng, X. Liu, Y. Xiang, *J. Phys. Chem. C* **2024**, *128*, 18659.
[106] Q. Wang, C. Zhao, J. Wang, Z. Yao, S. Wang, S. G. H. Kumar, S. Ganapathy, S. Eustace, X. Bai, B. Li, M. Wagemaker, *Nat. Commun.* **2023**, *14*, 440.
[107] Z. Liang, Y. Xiang, K. Wang, J. Zhu, Y. Jin, H. Wang, B. Zheng, Z. Chen, M. Tao, X. Liu, Y. Wu, R. Fu, C. Wang, M. Winter, Y. Yang, *Nat. Commun.* **2023**, *14*, 259.
[108] A. B. Gunnarsdóttir, C. V. Amanchukwu, S. Menkin, C. P. Grey, *J. Am. Chem. Soc.* **2020**, *142*, 20814.
[109] Y. Kwon, A. Svirinovsky-Arbeli, J. C. Hestenes, P. J. Buitrago Botero, K. R. M. Corpus, P. Lepucki, O. Pecher, L. E. Marbella, *Chem* **2024**, *10*, 3159.
[110] Q. Wang, C. Zhao, S. Wang, J. Wang, M. Liu, S. Ganapathy, X. Bai, B. Li, M. Wagemaker, *J. Am. Chem. Soc.* **2022**, *144*, 21961.
[111] X. Lin, Y. Shen, Y. Yu, Y. Huang, *Adv. Energy Mater.* **2024**, *14*, 2303918.
[112] M. Tao, X. Chen, H. Lin, Y. Jin, P. Shan, D. Zhao, M. Gao, Z. Liang, Y. Yang, *ACS Nano* **2023**, *17*, 24104.
[113] X. Cheng, F. Xian, Z. Hu, C. Wang, X. Du, H. Zhang, S. Chen, S. Dong, G. Cui, *Angew. Chem., Int. Ed.* **2019**, *58*, 5936.
[114] M. Wang, H. Liang, C. Wang, A. Wang, Y. Song, J. Wang, B. Wang, Y. Wei, X. He, Y. Yang, *Adv. Mater.* **2023**, *35*, 2306683.
[115] M. Wang, H. Liang, L. Wang, H. Zhang, J. Wang, Y. Wei, X. He, Y. Yang, *Matter* **2022**, *5*, 3530.
[116] R. Zhang, X. Shen, Y.-T. Zhang, X.-L. Zhong, H.-T. Ju, T.-X. Huang, X. Chen, J.-D. Zhang, J.-Q. Huang, *J. Energy Chem.* **2022**, *71*, 29.
[117] S. Xu, K.-H. Chen, N. P. Dasgupta, J. B. Siegel, A. G. Stefanopoulou, *J. Electrochem. Soc.* **2019**, *166*, A3456.
[118] D. Tewari, S. P. Rangarajan, P. B. Balbuena, Y. Barsukov, P. P. Mukherjee, *J. Phys. Chem. C* **2020**, *124*, 6502.
[119] R. A. Vilá, D. T. Boyle, A. Dai, W. Zhang, P. Sayavong, Y. Ye, Y. Yang, J. A. Dionne, Y. L. H. Cui, *Sci. Adv.* **2025**, *9*, eadf3609.
[120] M. J. Zachman, Z. Tu, S. Choudhury, L. A. Archer, L. F. Kourkoutis, *Nature* **2018**, *560*, 345.
[121] Y. Lin, H. Zhang, L. Liu, J. Wang, *Energy Fuels* **2024**, *38*, 17241.
[122] G. Xu, X. Du, S. Zhang, J. Li, S. Dong, Z. Hu, G. Cui, *Interdiscip. Mater.* **2023**, *2*, 337.
[123] H. Wang, X. Yan, R. Zhang, J. Sun, F. Feng, H. Li, J. Liang, Y. Wang, G. Ye, X. Luo, S. Huang, P. Wan, S. T. Hung, F. Ye, F. Chen, E. Wu, J. Zhou, U. Ulissi, X. Ge, C. Liu, B. Xu, N. Liu, C. Ouyang, *Nat. Nanotechnol.* **2025**, *20*, 1034.
[124] R. Bhattacharyya, B. Key, H. Chen, A. S. Best, A. F. Hollenkamp, C. P. Grey, *Nat. Mater.* **2010**, *9*, 504.
[125] F. Aguesse, W. Manalastas, L. Buannic, J. M. Lopez del Amo, G. Singh, A. Llordés, J. Kilner, *ACS Appl. Mater. Interfaces* **2017**, *9*, 3808.
[126] Y.-C. Hsieh, M. Leißing, S. Nowak, B.-J. Hwang, M. Winter, G. Brunklaus, *Cell Rep. Phys. Sci.* **2020**, *1*, 100139.
[127] A. B. Gunnarsdóttir, S. Vema, S. Menkin, L. E. Marbella, C. P. Grey, *J. Mater. Chem. A* **2020**, *8*, 14975.
[128] M. A. Hope, B. L. D. Rinkel, A. B. Gunnarsdóttir, K. Märker, S. Menkin, S. Paul, I. V. Sergeyev, C. P. Grey, *Nat. Commun.* **2020**, *11*, 2224.
[129] A. Maity, A. Svirinovsky-Arbeli, Y. Buganim, C. Oppenheim, M. Leskes, *Nat. Commun.* **2024**, *15*, 9956.
[130] N. Li, J. You, Y. Gao, F. Qiao, Y. Yang, T. Jin, C. Shen, H. Huang, K. Xie, *InfoMat* **2023**, *5*, e12402.
[131] F. Liu, R. Xu, Y. Wu, D. T. Boyle, A. Yang, J. Xu, Y. Zhu, Y. Ye, Z. Yu, Z. Zhang, X. Xiao, W. Huang, H. Wang, H. Chen, Y. Cui, *Nature* **2021**, *600*, 659.
[132] W. Zhang, P. Sayavong, X. Xiao, S. T. Oyakhire, S. B. Shuchi, R. A. Vilá, D. T. Boyle, S. C. Kim, M. S. Kim, S. E. Holmes, Y. Ye, D. Li, S. F. Bent, Y. Cui, *Nature* **2024**, *626*, 306.
[133] L. Li, S. Basu, Y. Wang, Z. Chen, P. Hundekar, B. Wang, J. Shi, Y. Shi, S. Narayanan, N. Koratkar, *Science* **2018**, *359*, 1513.
[134] C. Jin, O. Sheng, G. Wei, H. Li, Q. Han, Q. Zhang, X. Tao, *Nat. Rev. Chem.* **2025**, *9*, 553.
[135] C. Jin, T. Liu, O. Sheng, M. Li, T. Liu, Y. Yuan, J. Nai, Z. Ju, W. Zhang, Y. Liu, Y. Wang, Z. Lin, J. Lu, X. Tao, *Nat. Energy* **2021**, *6*, 378.
[136] Y. Zhang, J. Liu, Y. Li, D. Zhao, W. Huang, Y. Zheng, J. Zhou, C. Zhu, C. Deng, Y. Sun, T. Qian, C. Yan, *Adv. Funct. Mater.* **2023**, *33*, 2301332.
[137] J. Chen, Z. Cheng, Y. Liao, L. Yuan, Z. Li, Y. Huang, *Adv. Energy Mater.* **2022**, *12*, 2201800.
[138] L. Dong, S. Zhong, B. Yuan, Y. Li, J. Liu, Y. Ji, D. Chen, Y. Liu, C. Yang, J. Han, W. He, *Angew. Chem., Int. Ed.* **2023**, *62*, e202301073.
[139] Z. M. Konz, B. D. McCloskey, *Nat. Energy* **2022**, *7*, 1005.

Manuscript received: June 15, 2025
Revised manuscript received: August 11, 2025
Version of record online: September 9, 2025